The Cryosphere, 15, 3555–3575, 2021
https://doi.org/10.5194/tc-15-3555-2021

The Cryosphere Open Access EGU

Recent degradation of interior Alaska permafrost mapped with ground surveys, geophysics, deep drilling, and repeat airborne lidar

Thomas A. Douglas[1], Christopher A. Hiemstra[1,a], John E. Anderson[2], Robyn A. Barbato[3], Kevin L. Bjella[1], Elias J. Deeb[3], Arthur B. Gelvin[1], Patricia E. Nelsen[1], Stephen D. Newman[3], Stephanie P. Saari[1], and Anna M. Wagner[1]

[1]U.S. Army Cold Regions Research and Engineering Laboratory, 9th Avenue, Building 4070, Fort Wainwright, AK 99709, USA
[2]U.S. Army Geospatial Research Laboratory, Corbin Field Station 15315 Magnetic Lane, Woodford, VA 22580, USA
[3]U.S. Army Cold Regions Research and Engineering Laboratory, 72 Lyme Road, Hanover, NH 03755, USA
[a]now at: US Department of Agriculture, Forest Service, Geospatial Management Office, Salt Lake City, UT 84138, USA

Correspondence: Thomas A. Douglas (thomas.a.douglas@usace.army.mil)

Received: 9 February 2021 – Discussion started: 22 February 2021
Revised: 14 May 2021 – Accepted: 18 May 2021 – Published: 3 August 2021

Abstract. Permafrost underlies one-quarter of the Northern Hemisphere but is at increasing risk of thaw from climate warming. Recent studies across the Arctic have identified areas of rapid permafrost degradation from both top-down and lateral thaw. Of particular concern is thawing syngenetic "yedoma" permafrost which is ice-rich and has a high carbon content. This type of permafrost is common in the region around Fairbanks, Alaska, and across central Alaska expanding westward to the Seward Peninsula. A major knowledge gap is relating belowground measurements of seasonal thaw, permafrost characteristics, and residual thaw layer development with aboveground ecotype properties and thermokarst expansion that can readily quantify vegetation cover and track surface elevation changes over time. This study was conducted from 2013 to 2020 along four 400 to 500 m long transects near Fairbanks, Alaska. Repeat active layer depths, near-surface permafrost temperature measurements, electrical resistivity tomography (ERT), deep (> 5 m) boreholes, and repeat airborne light detection and ranging (lidar) were used to measure top-down permafrost thaw and map thermokarst development at the sites. Our study confirms previous work using ERT to map surface thawed zones; however, our deep boreholes confirm the boundaries between frozen and thawed zones that are needed to model top-down, lateral, and bottom-up thaw. At disturbed sites seasonal thaw increased up to 25 % between mid-August and early October and suggests measurements to evaluate active layer depth must be made as late in the fall season as possible because the projected increase in the summer season of just a few weeks could lead to significant additional thaw. At our sites, tussock tundra and spruce forest are associated with the lowest mean annual near-surface permafrost temperatures while mixed-forest ecotypes are the warmest and exhibit the highest degree of recent temperature warming and thaw degradation. Thermokarst features, residual thaw layers, and taliks have been identified at all sites. Our measurements, when combined with longer-term records from yedoma across the 500 000 km^2 area of central Alaska, show widespread near-surface permafrost thaw since 2010. Projecting our thaw depth increases, by ecotype, across the yedoma domain, we calculate a first-order estimate that 0.44 Pg of organic carbon in permafrost soil has thawed over the past 7 years, which, for perspective, is an amount of carbon nearly equal to the yearly CO_2 emissions of Australia. Since the yedoma permafrost and the variety of ecotypes at our sites represent much of the Arctic and subarctic land cover, this study shows remote sensing measurements, top-down and bottom-up thermal modeling, and ground-based surveys can be used predictively to identify areas of the highest risk for permafrost thaw from projected future climate warming.

Published by Copernicus Publications on behalf of the European Geosciences Union.

1 Introduction

Permafrost underlies ∼ 40 % of central Alaska, a 500 000 km^2 region stretching east to west from the Canadian border to the Seward Peninsula and north to south from the Brooks Range to the Alaska Range. This is expected to mostly disappear from the near surface (upper 1 m) by 2100 (Pastick et al., 2015). Mean annual air temperatures in interior Alaska, currently roughly −2 °C (Jorgenson et al., 2020), are projected to increase by 2 °C by 2050 (Douglas et al., 2014) and 5 °C by 2100 (Lader et al., 2017). Roughly half of the discontinuous permafrost in the area represents late Pleistocene ice and organic-carbon-rich "yedoma" (Kanevskiy et al., 2011; Strauss et al., 2016). In total, yedoma contains almost a third of the permafrost carbon pool despite underlying only 625 000 km^2 of central Alaska and Russia, ∼ 7 % of the total global permafrost land area (Heslop et al., 2019). Yedoma permafrost contains large organic carbon stocks that are extremely biolabile (Vonk et al., 2013; Strauss et al., 2017; Heslop et al., 2019) and highly vulnerable to thaw due to high ice content and the prevalence of massive ice bodies, particularly ice wedges (Strauss et al., 2013, 2017).

Throughout much of central Alaska the permafrost is undergoing widespread top-down and lateral thaw (Jorgensen et al., 2013, 2020; Douglas et al., 2020; Circumpolar Active Layer Monitoring Network, 2020). Recent measurements of lateral thaw (Neumann et al., 2019) and modeled bottom-up thaw (McClymont et al., 2013; Way et al., 2018) of discontinuous permafrost bodies have also been reported. Permafrost degradation alters hydrogeology, soils, vegetation, and microbial communities (Racine and Walters, 1994; Walker et al., 2006; Mackelprang et al., 2011, 2017; Wilhelm et al., 2011; Wolken et al., 2011; Messan et al., 2020). Microbiological and trace metal processes are also likely to change in thawing permafrost ecosystems due to alterations in soil, vegetation, and wetland properties (Grosse et al., 2011; Douglas et al., 2013; Schuster et al., 2018; Burkert et al., 2019). In addition to these ecological and hydrologic changes, permafrost degradation presents an expensive and uncertain challenge for the design, siting, and maintenance of vertical and horizontal infrastructure in cold regions (Hjort et al., 2018).

The thermal state of near-surface permafrost is controlled by topography, slope, aspect, soil texture, ground ice content, air temperature, hydrology, land cover, snow depth and timing, and liquid precipitation (Osterkamp and Romanovsky, 1999; Jorgenson and Osterkamp, 2005; Myers-Smith et al., 2008; Loranty et al., 2018). In relatively warm areas like interior Alaska, the permafrost is "ecosystem protected" (Shur and Jorgenson, 2007) by an insulating organic-rich soil, plant litter, and vegetation surface layer. Disturbance to this insulating layer from climate warming, infrastructure development, or wildfire increases ground heat flux and promotes top-down, lateral, and bottom-up thaw (Viereck et al., 1973; Yoshikawa et al., 2003; Nossov et al., 2013).

Commonly, the first signal of an altered permafrost thermal state is an increased seasonally thawed active layer (Hinkel et al., 2003; Shiklomonov et al., 2010). Seasonal trends in active layer depth, particularly across a variety of ecotypes, can provide information on how and where permafrost degradation features initiate and expand. Low-ice-content dry sandy soils typically have deeper active layers than ice-rich silt or organic-rich soils (Brown et al., 2015; Loranty et al., 2018). As such, active layer measurements can infer information about subsurface soil characteristics. When top-down permafrost degradation occurs, the active layer depth may increase before any readily identifiable change in surface vegetation or geomorphology occurs. The most pronounced terrain surface features form when thaw of ice-rich permafrost leads to thermokarst (hollows formed by ground subsidence following thaw of ice-rich permafrost; Kokelj and Jorgenson, 2013; Brown et al., 2015; Douglas et al., 2016). Thermokarst features include lakes, bogs, fens, and pits in lowlands and thaw slumps and active layer detachments in uplands (Smith et al., 2005; Jorgenson et al., 2013).

There is a need to broadly apply remotely sensed analyses to identify high-ice-content permafrost at risk of top-down and lateral thaw degradation to support ecological, hydrologic, and engineering investigations. Identifying risk factors for thermokarst initiation typically requires combining ground-based surveys and remotely sensed measurements. Where permafrost is associated with surface biophysical characteristics that can be measured remotely, standoff detection tools like airborne lidar and repeat imagery analysis can be applied toward tracking trajectories of change over large regions (Jones et al., 2013; Chasmer and Hopkinson, 2016; Lewkowicz and Way, 2019). Geophysical techniques, predominantly electrical resistivity tomography (ERT), have been recently coupled with airborne and active layer measurements to detect thermokarst development and associate ice content with terrain geomorphology (Yoshikawa et al., 2006; Douglas et al., 2008; Lewkowicz et al., 2011; Hubbard et al., 2013; Minsley et al., 2015; Bjella, 2020) and biophysical characteristics (Douglas et al., 2016) at broader scales. A combination of repeat active layer measurements, geophysical surveys, and airborne lidar have been used to map subsurface permafrost bodies, quantify top-down thaw, and identify locations where thermokarst features have been initiated or expanded (Douglas et al., 2016; Rey et al., 2020). Long-term ground-based time series measurements can be combined with ERT to quantify top-down thaw, track the initiation and lateral expansion of thermokarst features, and identify where ecosystem characteristics influence the permafrost thermal regime. Furthermore, extents of the base and sides of discontinuous permafrost bodies, confirmed with geophysical measurements and deep boreholes, are needed to monitor and better model lateral and bottom-up thaw.

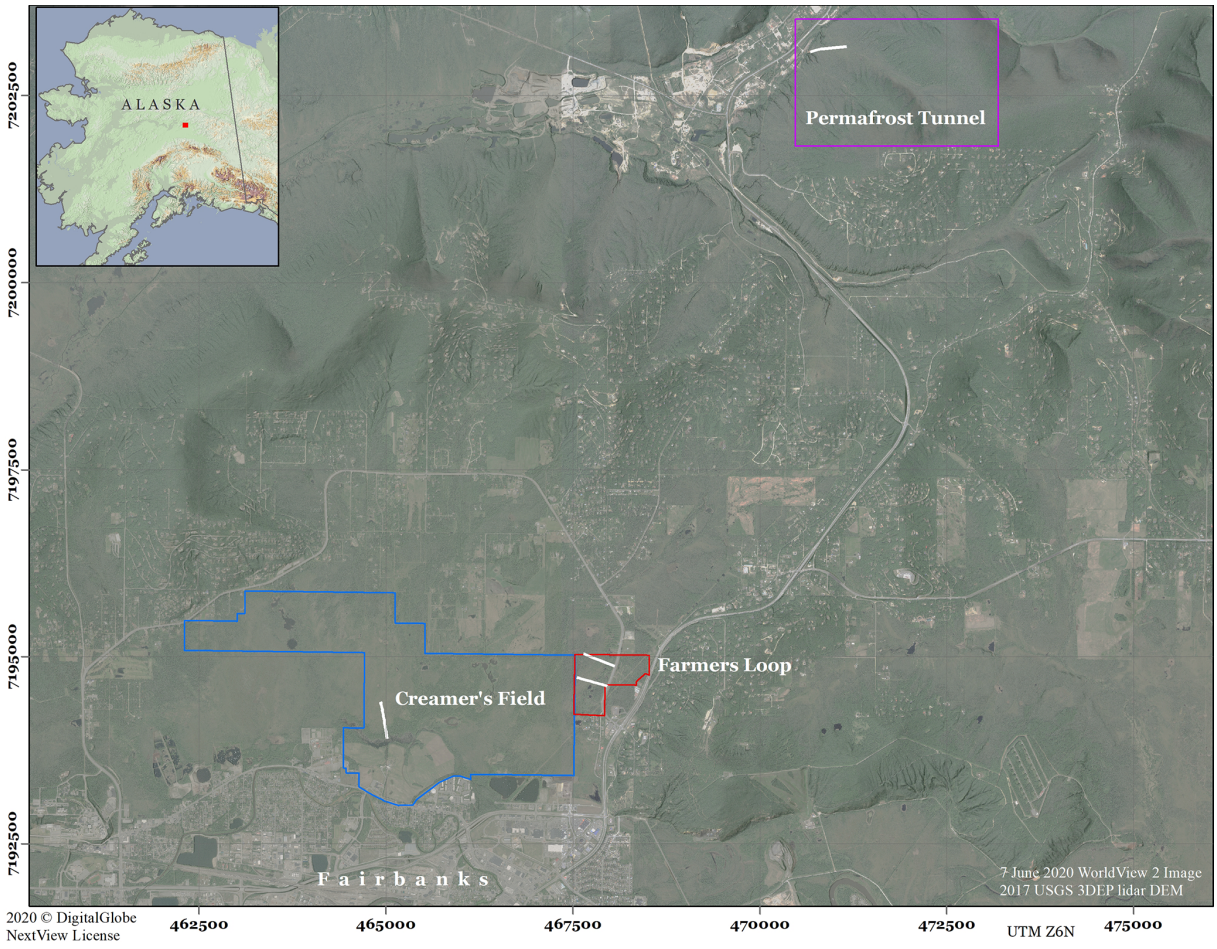

Figure 1. A WorldView-2 (© Digital Globe) satellite image of the area around Fairbanks, Alaska (red dot on inset map), identifying the field sites (colored regions) and transects (white lines) in this study.

The objective of this study was to establish relationships between ecotype, permafrost soil characteristics, and seasonal thaw across a variety of terrains in interior Alaska. Our sites represent 159 000 km^2 of high-ice-content yedoma permafrost with massive ice wedges that is present across the 500 000 km^2 expanse of central Alaska (Strauss et al., 2016). We made repeat seasonal and active layer thaw depth measurements, performed electrical resistivity tomography, and characterized the permafrost with boreholes up to 15 m deep along transects that represent the five most common ecotypes associated with central Alaska's yedoma permafrost. Ground-based information was combined with high-resolution repeat airborne lidar imagery to identify thermokarst initiation and quantify terrain elevation changes over time. Long-term active layer depth measurements across central Alaska were used to place our measurements into spatially broader and temporally longer scales. We used our active layer–ecotype relationships to model the amount of yedoma permafrost carbon that has thawed across central Alaska since 2013. The goals of this work were to measure seasonal thaw and thermokarst development over time and identify surface and subsurface terrain properties that can be remotely quantified, like vegetation type and thaw subsidence, with permafrost geophysical, soil, and active layer characteristics.

2 Study area

Our field sites are located near Fairbanks, Alaska (Fig. 1). The region has a continental climate with a mean annual air temperature of −2.4 °C, typical mean summer temperatures of 20 °C, mean winter temperatures of −20 °C, and yearly extremes ranging from −51 to 38 °C (Jorgenson et al., 2001, 2020). Mean annual precipitation is 28.0 cm (Wendler and Shulski, 2009) with a typical annual snowfall of 1.7 m (Jorgenson et al., 2001) that represents 40 %–45 % of the annual precipitation (Liston and Hiemstra, 2011). Discontinuous permafrost features in the area are up to 60 m thick and are located primarily in lowlands, along north-facing slopes, and where soils or vegetation provide adequate thermal pro-

tection (Racine and Walters, 1994; Jorgenson et al., 2008; Douglas et al., 2014). Permafrost at our field sites is Pleistocene syngenetic ice-rich yedoma formed through repeated deposition of windblown loess and organic matter (Shur and Jorgenson, 2007; Douglas et al., 2011; Strauss et al., 2016). Almost a third (181 000 km^2) of the global yedoma permafrost is in Alaska, and of that the majority is in a swath of central Alaska between the Brooks Range to the north and the Alaska Range to the south (Strauss et al., 2016). Carbon content in the permafrost of 2 %–5 % ($\sim 10\,kg\,m^{-3}$) is up to 30 times greater than unfrozen mineral soil (Strauss et al., 2013).

Our field investigations were organized along four transects crossing a variety of lowland ($n = 3$) and upland ($n = 1$) permafrost landscapes (Fig. 1). The 400 m "Farmer's Loop 1" and 500 m "Farmer's Loop 2" transects were located at 64.877° N, 147.674° W and 64.874° N, 147.677° W, respectively. These sites are part of the Cold Regions Research and Engineering Laboratory (CRREL) Farmer's Loop permafrost experimental test site. These two transects cross a variety of ecotypes including mixed deciduous forest (dominated by *Picea glauca* and *Betula neoalaskana*), *Salix* spp. riparian wetland, *Eriophorum vaginatum* tussock tundra, and black spruce (*Picea mariana*) forest with a ground cover of moss (*Sphagnum* spp.). Trail crossings and other clearings (disturbed areas), devoid of trees, punctuate the transects in multiple locations and are inhabited by the grass *Calamagrostis canadensis*. A nearby Circumpolar Active Layer Monitoring (CALM) site has a 16-year active layer record (CALM, 2020). A 500 m transect at the nearby Creamer's Field Migratory Waterfowl Refuge (64.868° N, 147.738° W) transitions from mixed deciduous forest (*Betula neoalaskana* and *P. glauca*) in the first 150 m before entering moss–black spruce forest for ~ 50 m. Farther north on this transect *Eriophorum vaginatum* tussock tundra is prevalent with isolated *B. neoalaskana* and *P. mariana* trees along with two east–west-oriented trail crossings. A 400 m southwest–northeast-oriented transect was also established above the CRREL Permafrost Tunnel in Fox, Alaska (64.950° N, 147.621° W). Vegetation at this site transitions from black spruce forest with moss through 1960s-era clearings and trails and shrub-dominated (*Rhododendron groenlandicum* and *Betula nana)* clearings into Glenn Creek's riparian zone. Our field sites encompass common boreal ecoregion land cover classes (subpolar needleleaf and deciduous forest, mixed forest, shrubland, grassland, wetland, barren, disturbed, and water). Together, these classes account for 74 % of the boreal ecoregion's area in North America (Latifovic et al., 2017).

3 Material and methods

3.1 Satellite and lidar imagery

Imagery was needed to examine transect land cover types corresponding with lidar data. Cloud-free high-resolution Maxar WorldView-2 (WV 2) satellite imagery (2 m multispectral; 0.5 m panchromatic) was obtained for all sites (Fig. 1) on 7 June 2020. The images were orthorectified and pan-sharpened using ENVI's 5.5.3 SPEAR pan-sharpening (Gram-Schmidt) to qualitatively maximize the imagery to match lidar data. Airborne lidar measurements, helpful for monitoring surface changes and examining surface roughness characteristics, were acquired in 2010 and 2020, and for each collection the aircraft and sensor position and altitude data were indexed by GPS time for post-processing correction and calibration. Lidar data were collected on 5–6 May 2010 for just the Creamers Field Transect using an Optech (Toronto, Canada) ALTM Gemini 1064 nm lidar with a pulse frequency of 70 kHz and 12° scan angle, and the resulting point cloud (point density = 4 points m^{-2}) was used to create a 1.21 m resolution digital elevation model (DEM) with a vertical accuracy of 16 cm (Hubbard et al., 2011). In 2020, all three of the sites (Fig. 1) were scanned between 17–18 May with a Leica (Wetzlar, Germany) ALS80 1064 nm lidar with a pulse frequency of 490 kHz and 14° scan angle that acquired surface returns at an average density of ≥ 25 points m^{-2}. Each point cloud was processed to create a hydro-flattened raster surface with a spatial resolution of 0.25 m and vertical root mean square (rms) of ≤ 6.6. Hydro-flattening removes errant point cloud elevation artifacts from resulting DEMs given water's low reflectance. In this process, stream, pond, and lake boundaries are identified and the DEM was corrected to more accurately portray water level elevation given the identified shoreline, yielding a waterbody-smoothed product. Changes in elevation at the Creamer's Field site between 2010 and 2020 were calculated by subtracting 2010 elevations from 2020 elevations (2020 minus 2010) using raster algebra to delineate elevation losses (negative values) and gains (positive values) over the 10-year period. The 2020 data were resampled to the 1.21 m resolution of the 2010 data using bilinear interpolation for the comparison. The resolution of the difference raster is 1.21 m, the resolution of the coarsest dataset.

3.2 Field survey measurements, coring, and meteorology

In May–June 2013, 1 m wide trails were delicately hand cleared of large woody vegetation along linear transects to improve access for repeat surveying and geophysical measurements. A Trimble (Sunnyvale, California USA) R8 DGPS was used to survey pin flag measurement markers at a 4 m spacing along each of the four transects. We used a 1 cm diameter 1.7 m long graduated metal rod ("frost probe")

to make seasonal thaw depth measurements at each flag location to quantify the end of summer season active layer (Shiklomonov et al., 2013). Measurements were repeated in mid-October from 2013 to 2020. In 2014 additional measurements were made in June, July, and August. Active layer measurements from 2013 to 2017 were published previously (Douglas et al., 2020).

A Geoprobe 7822 direct push technology track-mounted drill rig was used to collect continuous cores to depths that ranged from 4 to 15.6 m in late winter and spring 2014. Coring was limited to locations that had trail access for the heavy tracked vehicle. Three wood fragments found in cores from the Farmer's Loop transects were analyzed for ^{14}C age and $\delta^{13}C$ measurements following commonly used radiocarbon analytical procedures at Geochron Laboratories (Chelmsford, Massachusetts, USA). A SIPRE corer was used to collect 2 to 3 m deep cores in the spring of 2017 and 2018 at locations representing the major ecotypes at each site following established methods (Douglas et al., 2011). Gravimetric (Geoprobe) or volumetric (SIPRE) moisture contents were measured following established methods (Phillips et al., 2015). Frozen bulk density (SIPRE cores; frozen mass divided by volume) and gravimetric moisture content (Geoprobe cores; mass of water lost through drying divided by volume) from the cores are included in Table S1.

An Onset (Bourne, Massachusetts, USA) HOBO U23 Pro v2 external temperature and relative humidity logger with a solar radiation shield was installed 2 m above the ground surface at the Permafrost Tunnel and Farmer's Loop sites. Onset HOBO U23 Pro v2 two-channel external temperature loggers were installed at depths of 1.2 m at nine locations across our field sites at locations where this depth represents permafrost. The thermistor was protected by a plastic sleeve and installed in the ground after a 0.75 cm diameter hole was excavated using a slide hammer and rod.

3.3 Electrical resistivity tomography

We used an Advanced Geosciences Incorporated (Austin, Texas) "SuperSting" R8 eight-channel portable induced polarization galvanic earth resistivity meter for ERT surveys, which we combine with our ground-based measurements to help quantify top-down thaw and track the initiation and lateral expansion of thermokarst features. ERT measurements were conducted in midsummer 2013 using six cables, each with 14 take-out electrodes. Our electrode spacings of 2.5 to 4 m achieved a maximum subsurface penetration depth of $\sim$ 30 m. We used a dipole–dipole array because it represents spatial aspects of ice-rich terrain and provides horizontal resolution sufficient for detecting vertical structures in permafrost (Kneisel, 2006; Douglas et al., 2016). Contact resistance was measured at each electrode prior to initiating the survey to ensure cable connectivity. At rare instances when contact resistances were higher than 2000 Ω m, salt water was added around the electrode and contact resistance was re-measured until resistance fell below 2000 Ω m. Electrodes were typically 45 cm long, but electrodes up to 3 m in length were used in areas with thick vegetation mats or moss.

We used RES2DINV (Geotomo Software, Penang, Malaysia) to perform two-dimensional model interpretation. The software provides signal smoothing and constrains inversion with finite-difference forward modeling and quasi-Newton techniques (Loke and Barker, 1996; Loke et al., 2003). A least-squares inversion achieves convergence by comparing changes in rms quadratic error between two and five iterations, then three and five iterations, etc. Convergence was achieved when rms error values reached $\sim$ 10 % convergence and further iterations would not significantly lower the rms values.

4 Results

4.1 Satellite and lidar imagery

The four transects we studied contain five dominant ecotypes of the boreal biome and central Alaska yedoma terrain (mixed deciduous forest, wetlands, tussock tundra, moss-black spruce forest with a thick moss cover, and disturbed; Douglas et al., 2020). The Creamer's Field transect starts in birch forest, transitions to mixed forest, and at 140 m transitions abruptly to tussock tundra for the remainder of its 500 m length (Figs. 2a and 3a). Patterned ground (near-surface ice wedge polygons) is readily evident in the airborne lidar in the mixed forest along the first $\sim$ 150 m of the transect (Fig. 2b). This area is characterized by high-centered polygons with up to 2 m of local relief that form when ice wedges melt. When the transect transitions to tussock tundra, ice wedge polygons are no longer as strongly visible at the ground surface, yet polygonal ground is evident in true-color satellite imagery and airborne lidar throughout the remainder of the transect (Figs. 2a and 3a). Winter trails, dominated by native graminoids, are evident in the true-color and lidar images at 290 and 460 m.

There is subtle evidence of ice wedge polygons along the two transects at the Farmer's Loop field site (based on WV 2 satellite images and lidar; Figs. 4a, b, 5a, and b). Both transects start in mixed forest that extends for $\sim$ 120 m. Transect 1 crosses a small wetland feature at 80 m before transitioning to tussock tundra until 310 m. After a graminoid-dominated trail the ecotype changes to black spruce forest. Farmer's Loop 2 transect shifts from mixed forest to a flow through fen wetland from 120 to 170 m. After a trail crossing at 200 m the ecotype shifts abruptly to tussock tundra until the 400 m mark where a trail crossing separates the tussock tundra from mature black spruce forest.

Though ice wedges are present throughout the 300 m of subsurface passages that run partially below the Permafrost Tunnel transect, they are covered by a $\sim$ 5 m thick surface layer of Holocene silt (Hamilton et al., 1988) and a thick ve-

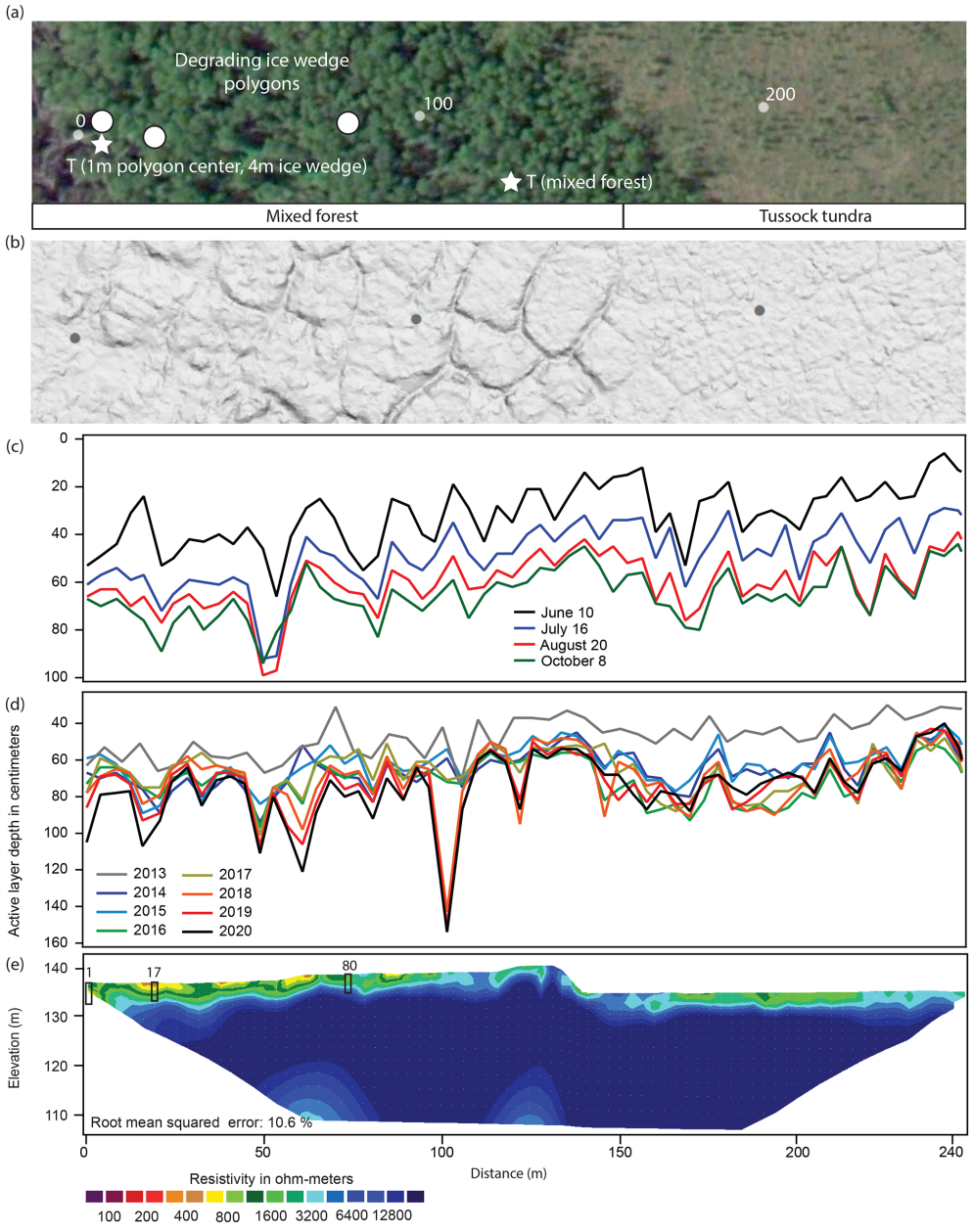

Figure 2. The Creamer's Field transect from 0 to 246 m (white line in Fig. 1). Panel **(a)** is a WorldView-2 (© Digital Globe) true-color image of the transect (white line) with terrain features and core locations (circles) identified, **(b)** lidar, **(c)** repeat thaw depth measurements in 2014, **(d)** repeat active layer depth measurements from 2013 to 2020, and **(e)** a 246 m electrical resistivity tomography transect corrected for ground surface elevation with boreholes identified as black boxes to true depth and numbers corresponding to the distance (in meters) of the borehole location along the transect. Stars with a "T" denote a thermistor location.

neer of mosses, lichen, shrubs, and trees. Polygonal ground is not identifiable in visible (WV 2) or lidar imagery at the surface along the Permafrost Tunnel transect (Fig. 6a and b). The Permafrost Tunnel transect originates in spruce forest, transits through shrubland, and crosses trails and Glenn Creek before entering black spruce forest again. Numerous trail crossings are visible and identified as disturbed locations, and a large thermokarst feature near Glenn Creek is also present. Anthropogenic features (i.e., disturbances) like roads, trails, and clearings are easily identifiable in the satellite imagery at all sites.

Our longest lidar data series spans May 2010 to 2020 and is limited to the Creamer's Field transect (Fig. 7). The differences in elevations from 2010 to 2020 indicate substantial elevation losses (over 1 m of subsidence) along the northern edge of degrading polygon ice wedges in an area that has

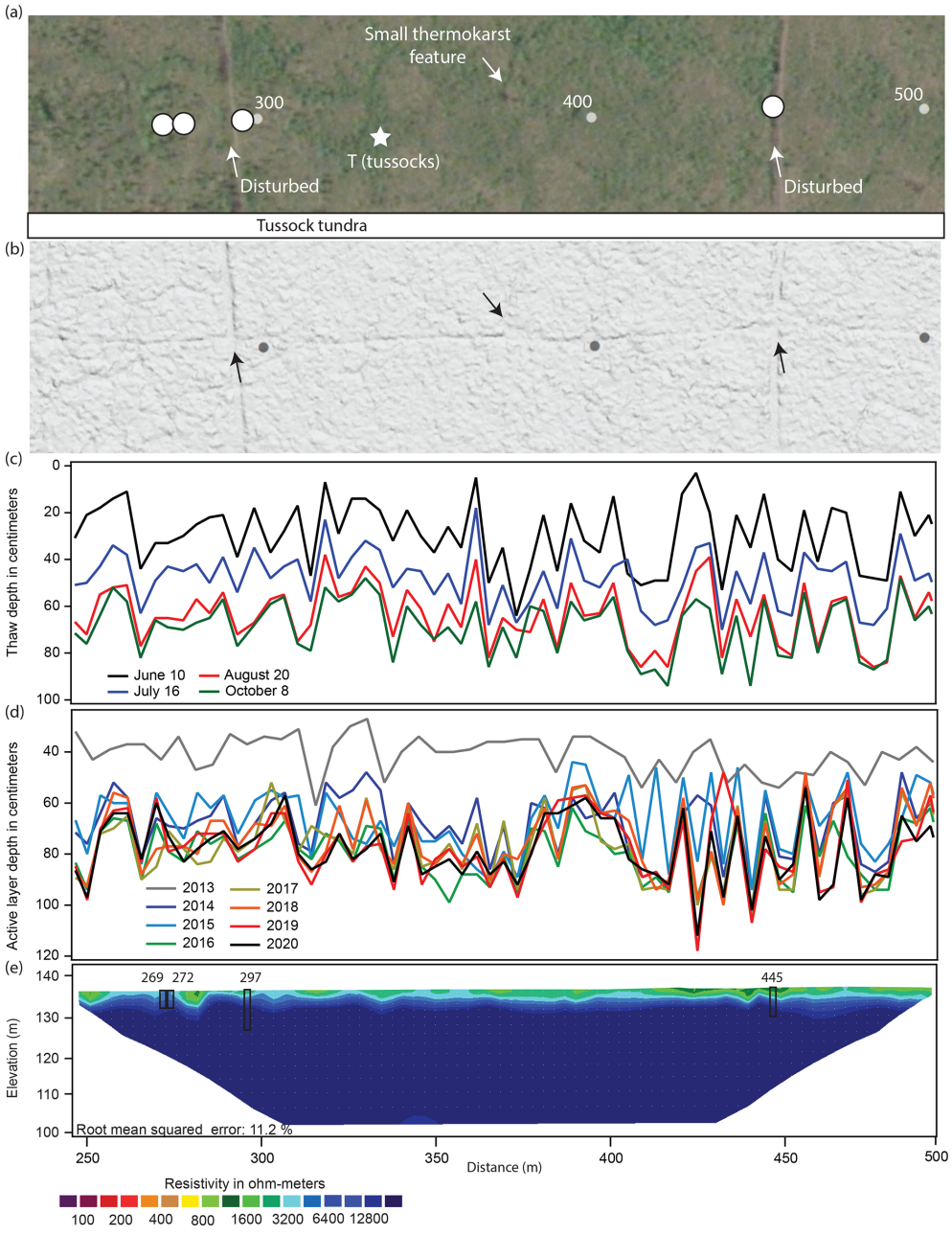

Figure 3. The Creamer's Field transect from 252 to 498 m (white line in Fig. 1). Panel **(a)** is a WorldView-2 (© Digital Globe) true-color image of the transect (white line) with terrain features and core locations (circles) identified, **(b)** May 2020 lidar, **(c)** repeat thaw depth measurements in 2014, **(d)** repeat active layer depth measurements from 2013 to 2020, and **(e)** a 246 m electrical resistivity tomography transect corrected for ground surface elevation with boreholes identified as black boxes to true depth and numbers corresponding to the distance (in meters) of the borehole location along the transect. Stars with a "T" denote a thermistor location.

transformed into an elongate lake. This thaw front of degrading permafrost is evident along the southern margin of the transect (left side of the map). Water levels in the pond and in some ice wedge polygon troughs show higher elevations in 2020 compared to 2010 (0.2 to 1.0 m) due to relatively higher summer rainfall in the last 3 years.

4.2 Field survey measurements, coring, and meteorology

The mid-June and early August seasonal thaw depth measurements and October active layer measurements in 2014 show a steady downward movement of the thaw front throughout the summer season (Figs. 2c, 3c, 4c, 5c, and 6c).

Table 1. A summary of the thaw depth measurements by ecotype and results from a means comparison using a Student *t* test. Among a given ecotype and different year, the letters identify statistically significantly different means. Mean values for a given ecotype and year with similar letters have similar means. *N* identifies the number of measurements in a given population.

	Year	*N*	Mean (cm)	Standard deviation (cm)	Statistically significant means	Percent increase 2013–2020
Tussock	2013	126	45.0	10.9	F	
	2014	153	67.7	12.2	D	50
	2015	153	63.3	12.6	E	41
	2016	153	75.3	12.1	A	67
	2017	153	72.2	13.8	B, C	60
	2018	153	69.5	13.3	C, D	54
	2019	153	72.8	13.9	A, B	62
	2020	153	73.5	13.4	A, B	63
Wetland	2013	41	71.5	24.4	D	
	2014	48	91.4	23.5	B, C	28
	2015	48	82.7	18.6	C, D	16
	2016	48	104.9	30.0	A, B	47
	2017	46	96.9	30.4	B, C	36
	2018	47	103.1	39.2	A, B	44
	2019	47	113.3	49.4	A	59
	2020	47	113.6	51.5	A	59
Disturbed	2013	35	75.5	23.8	C	
	2014	67	85.8	20.4	C	14
	2015	58	84.2	21.1	C	11
	2016	60	99.9	28.8	B	32
	2017	51	101.9	33.0	B	35
	2018	56	104.3	35.0	B	38
	2019	55	118.4	42.4	A	57
	2020	56	117.1	44.3	A	55
Mixed forest	2013	57	64.4	17.9	D	
	2014	75	81.4	19.0	B, C	27
	2015	75	75.1	17.2	C	17
	2016	75	85.1	27.1	B	32
	2017	75	79.5	24.0	B, C	24
	2018	74	84.9	25.7	B	32
	2019	74	93.4	29.0	A	45
	2020	74	97.4	30.2	A	51
Moss spruce	2013	86	54.6	13.3	E	
	2014	111	59.7	10.7	C, D	9
	2015	120	56.5	12.6	D, E	3
	2016	118	64.0	11.6	B	17
	2017	124	62.5	12.2	B, C	14
	2018	115	64.9	14.8	B	19
	2019	119	70.1	16.0	A	28
	2020	115	72.5	18.7	A	33

The majority ($\sim 80\,\%$) of the summer season thaw at the tussock tundra and spruce forest sites occurs by early August. However, in the wetland, disturbed, and mixed-forest ecotypes the increase in thaw depth from early August to mid-October is up to one-third of the eventual active layer depth. This is particularly evident along the first 200 m of the Farmer's Loop 2 transect (Fig. 5c). The wetland, disturbed, and mixed-forest ecotypes yield the deepest active layers at all sites. The tussock tundra and spruce with moss ecotypes consistently yield the lowest seasonal thaw measurements and show little change between August and October. A statistical summary of the active layer depths is provided in Table 1. It is clear that for all five ecotypes active layer depths increased substantially between 2013 and 2020. Since each

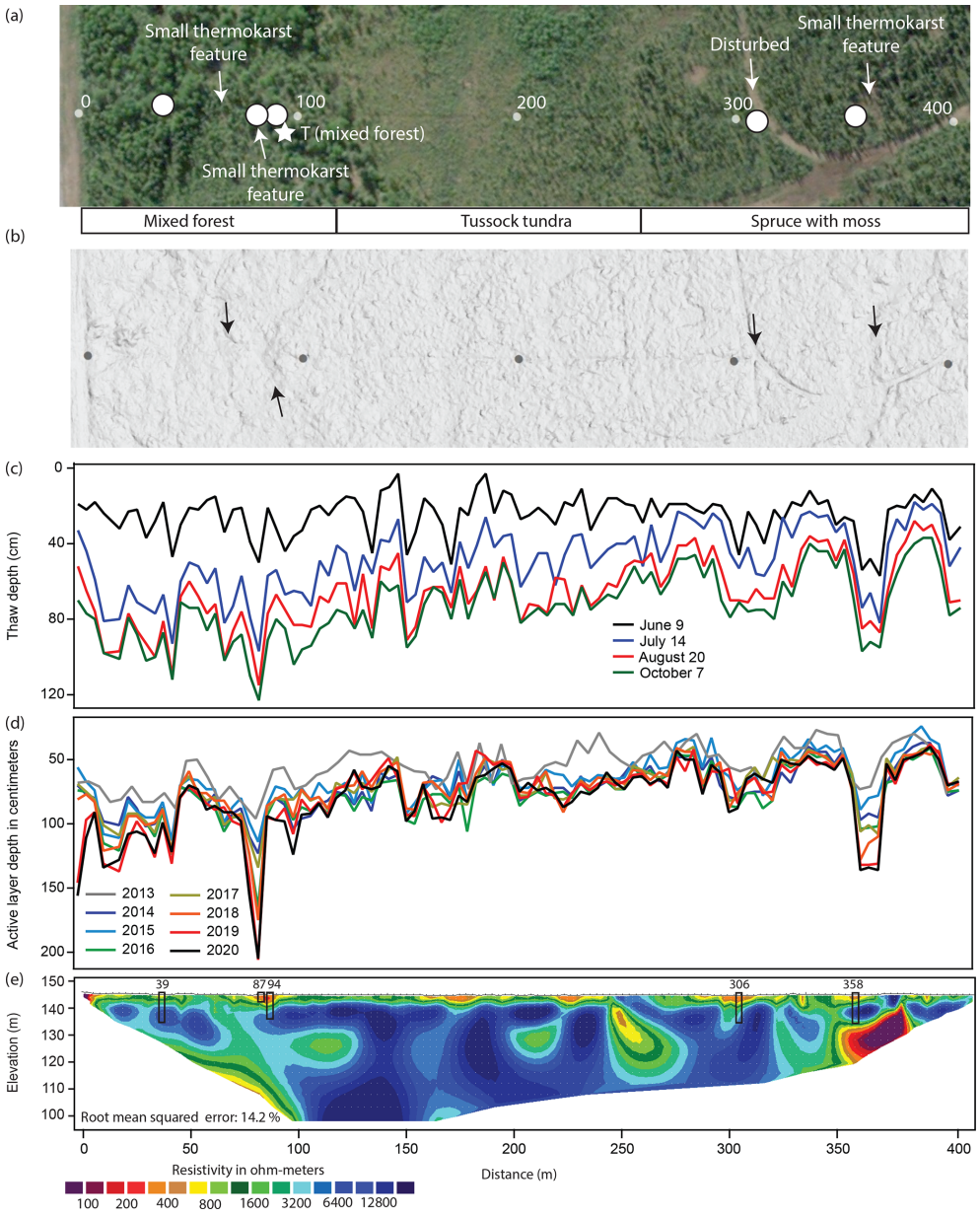

Figure 4. The Farmer's Loop 1 transect (white line in Fig. 1). Panel **(a)** is a WorldView-2 (© Digital Globe) true-color image of the transect (white line) with terrain features and core locations (circles) identified, **(b)** May 2020 lidar, **(c)** repeat thaw depth measurements in 2014, **(d)** repeat active layer depth measurements from 2013 to 2020, and **(e)** a 410 m electrical resistivity tomography transect corrected for ground surface elevation with boreholes identified as black boxes to true depth and numbers corresponding to the distance (in meters) of the borehole location along the transect. Stars with a "T" denote a thermistor location.

ecotype is associated with different starting thaw depths the percent increase in depth between 2013 and 2020 is a good indicator of top-down thaw over the 7-year period. The tussock, wetland, disturbed, and mixed-forest ecotypes all exhibited increases in active layer depth of more than 50 % while the increase in the spruce forest was 33 %. Across all five ecotypes the mean of active layer depth in 2013 was statistically significantly smaller than the measurement in 2020.

We collected 14 deep (greater than 5 m) cores with the Geoprobe and 12 shallow (3 m or less) SIPRE cores (Figs. 2d, 3d, 4d, 5d, and 6d). In general, the uppermost core samples, which consisted of surface vegetation and organic matter, yielded the greatest moisture content values. Most of the cores had peat or organic- and ice-rich permafrost in the upper 1–3 m and along some deeper sections, and these typically yielded gravimetric moisture contents greater than 100 %. The deeper permafrost soils were characterized as

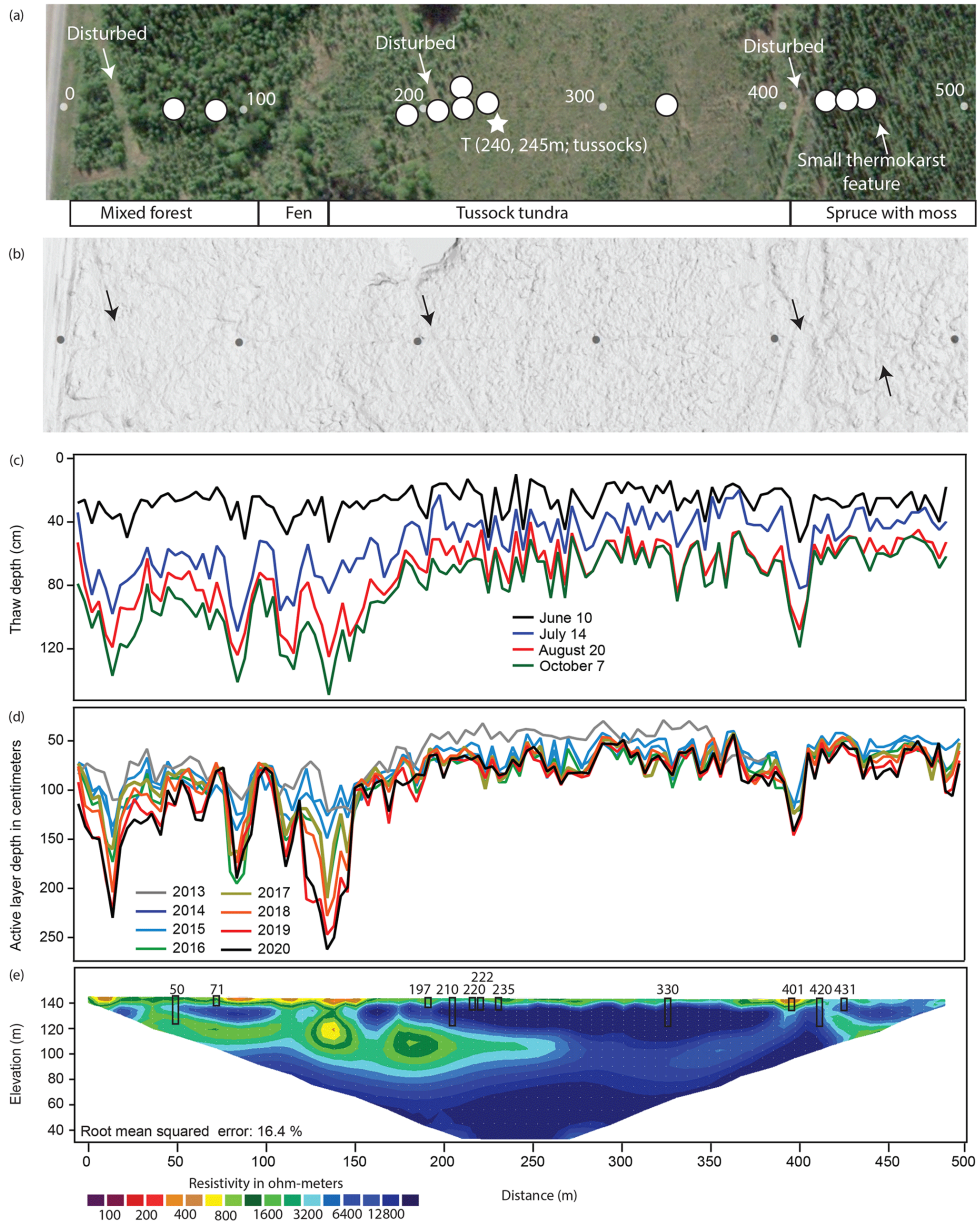

Figure 5. The Farmer's Loop 2 transect (white line in Fig. 1). Panel **(a)** is a WorldView-2 (© Digital Globe) true-color image of the transect (white line) with terrain features and core locations (circles) identified, **(b)** May 2020 lidar, **(c)** repeat thaw depth measurements in 2014, **(d)** repeat active layer depth measurements from 2013 to 2020, and **(e)** a 492 m electrical resistivity tomography transect corrected for ground surface elevation with boreholes identified as black boxes to true depth and numbers corresponding to the distance (in meters) of the borehole location along the transect. Stars with a "T" denote a thermistor location.

ice-rich to ice-poor silts and sands with gravimetric moisture contents of 60 %–150 %, which is similar to measurements of syngenetic yedoma-type permafrost in the Permafrost Tunnel (Bray et al., 2006; Douglas et al., 2011; Douglas and Mellon, 2019). For the subset of SIPRE cores that yielded frozen bulk densities, the values ranged predominantly between 900 and 1400 kg m^{-3}, which is also similar to values from the nearby Permafrost Tunnel; however, some ice-rich and peaty zones yielded values above 1400 kg m^{-3}.

Coring allowed us to confirm that large decreases in apparent resistivity values from ERT identified 0 °C isotherm boundaries between frozen and thawed material. Notably, a deep core at 358 m along the Farmer's Loop 1 transect yielded thawed silt from 9.15 to 10.35 m. The ERT measurements at that location show a large thawed region starting at $\sim$ 10 m depth identified by resistivity values of $\sim$ 1000 Ω m (more discussion below). Along the margins of most of the thawed zones we identified marked changes in apparent re-

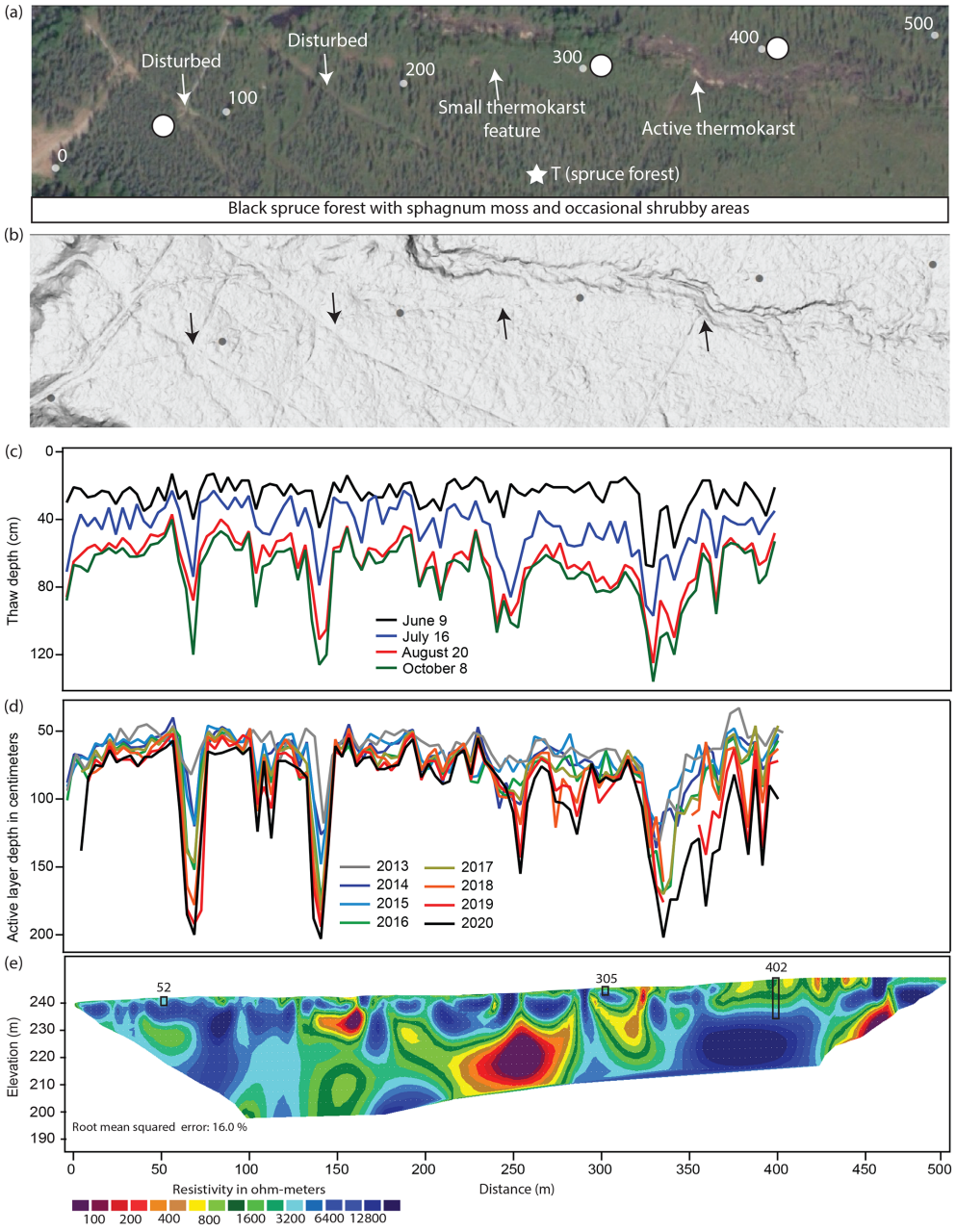

Figure 6. The Permafrost Tunnel transect (white line in Fig. 1). Panel **(a)** is a WorldView-2 (© Digital Globe) true-color image of the transect (white line) with terrain features and core locations (circles) identified, **(b)** May 2020 lidar, **(c)** repeat thaw depth measurements in 2014, **(d)** repeat active layer depth measurements from 2013 to 2020, and **(e)** a 410 m electrical resistivity tomography transect corrected for ground surface elevation with boreholes identified as black boxes to true depth and numbers corresponding to the distance (in meters) of the borehole location along the transect. Stars with a "T" denote a thermistor location.

sistivity that allowed identification of the lateral boundaries of thermokarst features. Notably, these include thawed zones in the high-centered polygons along the beginning of the Creamer's Field transect, thermokarst pits along the Farmer's Loop and Permafrost Tunnel transects, a large (∼ 50 m) lateral expansion of a thermokarst feature toward the end of the Permafrost Tunnel transect, and thawed regions below numerous disturbed areas at all sites. Some of the 2017 and 2018 SIPRE cores identified residual thaw layers between the bottom of the winter frozen layer and the top of the permafrost (Table S1). For example, a 2017 core from the mixed forest at 87 m along the Farmer's Loop 1 transect yielded thawed silt from to 46 to 102 cm. Cores collected in 2018 along the Farmer's Loop 2 transect in mixed forest at 71 m

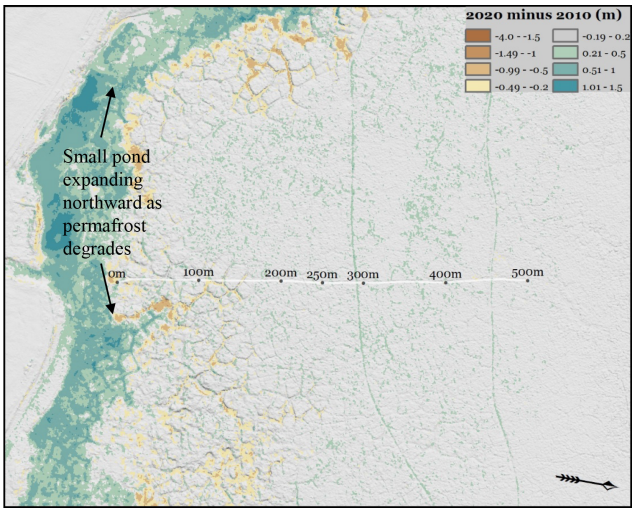

Figure 7. Past (2010) elevations were subtracted from current (2020) elevations at the Creamer's Field site (2020 minus 2010). The 500 m transect is denoted by the white line. Negative values identify regions of thaw degradation and subsidence over the 10-year period. Positive values show elevation gains due to deeper water and vegetation.

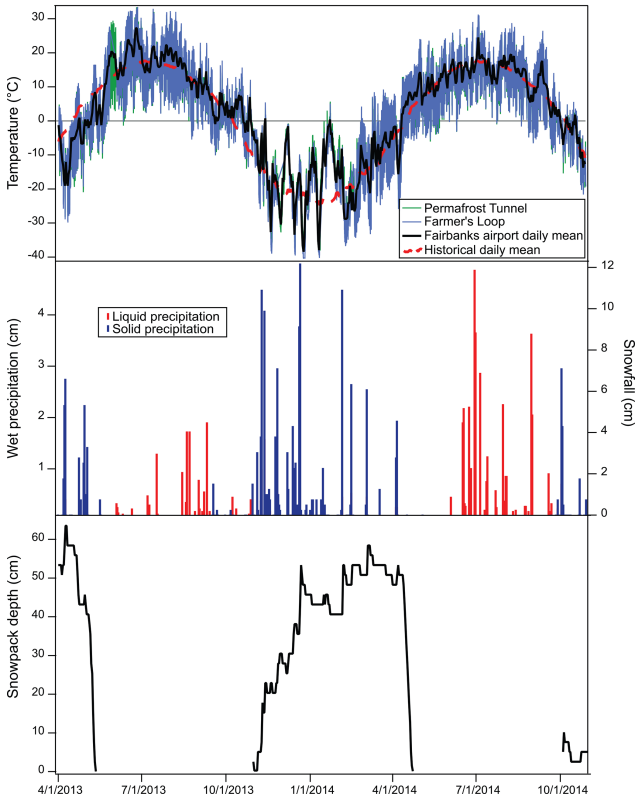

Figure 8. Meteorologic conditions from 1 April 2013 through 31 October 2014. **(a)** Air temperature from the Permafrost Tunnel and Farmer's Loop sites and historical daily mean values between 1929 and 2019 at the National Weather Service's Fairbanks International Airport (PAFA) site. **(b, c)** Precipitation at the PAFA site.

yielded thawed silt from 84 to 117 cm and two cores from the Permafrost Tunnel transect at 52 and 305 m yielded thawed silt from 31 to 49 cm and from 45 to 70 cm, respectively. These thawed zones are located above the typical permafrost table for those locations and indicate the active layer did not completely freeze back. Taliks are likely forming in those locations.

4.3 Radiocarbon dating

We obtained ^{14}C ages from wood fragments collected from three Geoprobe core samples through Geochron Laboratories (Chelmsford, Massachusetts, USA). An age of 10 360 ± 360 calibrated years before present (cal yr BP) (δ^{13}C: −27.7 ‰) was measured at a depth of 1.02 m in the tussock area at 306 m on the Farmer's Loop 1 transect (Table S1 in the Supplement). At 358 m along the same transect and also in the tussock area at 0.67 m depth, the ^{14}C age was 10 160 ± 160 cal yr BP (δ^{13}C: −28.0 ‰). Along the Farmer's Loop 2 transect, in the spruce forest at 420 m, and at a depth of 0.49 m, a wood fragment yielded a ^{14}C age of 7200 ± 190 cal yr BP (δ^{13}C: −28.7 ‰).

4.4 Air and ground temperature measurements

Air temperature, wet (rain) and dry (snow) total precipitation in centimeter, and the snowpack depth in centimeter, from 1 April 2013 through 31 October 2014, are provided in Fig. 8. This time period encompasses when the repeat summertime thaw depths and geophysical analyses were measured. The meteorological measurements were made by the National Weather Service at the Fairbanks International Airport (PAFA) 8 km to the southwest of the Creamer's Field and Farmer's Loop transects and 17 km southwest of the Permafrost Tunnel transect. Air temperatures at the Permafrost Tunnel and Farmer's Loop sites are also included, and they did not deviate substantially from one another or from the 90-year PAFA mean during the timeframe of the study. Air temperatures rose above 0 °C around the middle of May and did not go below freezing again until late October. The summer of 2013, when our ERT measurements were made, experienced a total of 14.5 cm of rainfall, which is slightly lower than the 90-year mean of 18.5 cm. The 2013 summer mean temperature of 12.2 °C was close to the 90-year summer mean of 11.8 °C. (Jorgenson et al., 2020). In terms of heating degree days, the summer of 2013 (1133) was slightly above the historical mean of 1090. The winter of 2013–2014 total snowfall of 1.22 m was slightly below the historical mean of 1.7 m. The wet precipitation total for the summer of 2014 (37.1 cm) was anomalously higher than the mean.

Figure 9 provides mean annual ground temperatures (MAGTs) at 1.2 m depth for locations that represent the range of ecotypes at our sites. In 2013, when the thermistors

Table 2. A summary of thermistor measurements from 1.2 m depth at the study site transects. Mean annual temperature (MAT) values for each of six individual years are presented as well as the 7-year global mean annual temperature for each site.

Creamer's Field, disturbed		MAT °C	Creamer's Field, 1 m polygon center		MAT °C	Creamer's Field, 1 m ice wedge in mixed forest		MAT °C
10/01/13	09/30/14	2.78	10/01/13	09/30/14	−0.36	10/01/13	09/30/14	−0.37
10/01/14	09/30/15	4.57	10/01/14	09/30/15	−0.29	10/01/14	09/30/15	−0.33
10/01/15	09/30/16	3.85	10/01/15	09/30/16	−0.26	10/01/15	09/30/16	−0.23
10/01/16	09/30/17	4.91	10/01/16	09/30/17	−0.23	10/01/16	09/30/17	−0.20
10/01/17	09/30/18	5.15	10/01/17	09/30/18	−0.16	10/01/17	09/30/18	−0.10
10/01/18	09/30/19	4.61	10/01/18	09/30/19	−0.13	10/01/18	09/30/19	−0.08
10/01/19	09/30/20	N/A	10/01/19	09/30/20	−0.11	10/01/19	09/30/20	−0.06
	7-year mean	4.31		7-year mean	−0.22		7-year mean	−0.20
Creamer's Field, mixed forest		MAT °C	Creamer's Field, tussocks		MAT °C	Farmer's Loop 1, mixed forest		MAT °C
10/01/13	09/30/14	−0.72	10/01/13	09/30/14	−2.85	10/01/13	09/30/14	−0.21
10/01/14	09/30/15	−0.20	10/01/14	09/30/15	−3.03	10/01/14	09/30/15	−0.08
10/01/15	09/30/16	−0.23	10/01/15	09/30/16	−1.63	10/01/15	09/30/16	−0.07
10/01/16	09/30/17	−0.15	10/01/16	09/30/17	−0.34	10/01/16	09/30/17	−0.04
10/01/17	09/30/18	−0.13	10/01/17	09/30/18	−0.51	10/01/17	09/30/18	−0.02
10/01/18	09/30/19	−0.12	10/01/18	09/30/19	−1.31	10/01/18	09/30/19	0.00
10/01/19	09/30/20	−0.11	10/01/19	09/30/20	−1.15	10/01/19	09/30/20	0.06
	7-year mean	−0.24		7-year mean	−1.55		7-year mean	−0.05
Farmer's Loop 2, 240 m tussocks		MAT °C	Farmer's Loop 2, 245 m tussocks		MAT °C	Permafrost Tunnel, spruce forest		MAT °C
10/01/13	09/30/14	−2.29	10/01/13	09/30/14	−3.70	10/01/13	09/30/14	−0.74
10/01/14	09/30/15	−2.62	10/01/14	09/30/15	−3.20	10/01/14	09/30/15	−1.17
10/01/15	09/30/16	−0.68	10/01/15	09/30/16	−2.16	10/01/15	09/30/16	−0.40
10/01/16	09/30/17	−1.45	10/01/16	09/30/17	−2.98	10/01/16	09/30/17	−0.98
10/01/17	09/30/18	−0.63	10/01/17	09/30/18	−1.80	10/01/17	09/30/18	−0.28
10/01/18	09/30/19	−0.55	10/01/18	09/30/19	−2.21	10/01/18	09/30/19	−0.27
10/01/19	09/30/20	−1.51	10/01/19	09/30/20	−2.16	10/01/19	09/30/20	−0.25
	7-year mean	−1.39		7-year mean	−2.60		7-year mean	−0.58

were installed, this depth represented the upper 40–60 cm of permafrost. We also provide the mean annual ground temperature at 1.2 m depth for each site between 1 October 2013 and 1 October 2019 (Table 2). The Creamer's Field disturbed site, in a clearing devoid of permafrost 114 m southeast of the Creamer's Field transect, is the only location where the mean annual soil temperature at 1.2 m is above freezing (4.31 °C). The remaining thermistors emplaced to 1.2 m depth are located in permafrost, and their temperatures remained below 0 °C for the entire record; however, they all show warming between 2013 and 2019. Thermistors in the mixed-forest and spruce forest ecotypes have been steadily approaching 0 °C. Mean annual permafrost temperatures at the two mixed-forest sites (−0.24 and −0.20 °C) and spruce forest (−0.25 °C) are substantially higher than for the three tussock tundra thermistor locations (−1.55, −1.39, and −2.60 °C). The tussock tundra sites also have the lowest winter permafrost temperatures.

4.5 Electrical resistivity tomography

Electrical resistivity tomography measurements across the transects (Figs. 2e, 3e, 4e, 5e, and 6e) provide insight into the presence or absence of permafrost at depths of up to 40 m below the ground surface, particularly when they are calibrated with subsurface information from boreholes. Resistivity values of ∼ 800 Ω m and higher have been reported for syngenetic permafrost near Fairbanks while values below 800 Ω m are generally assumed to represent thawed material (Hoekstra and McNeill, 1973; Harada et al., 2000; Yoshikawa et al., 2006; Douglas et al., 2008; 2016; Minsley et al., 2016). For the Creamer's Field transect (Figs. 2 and 3) the first 130 m consists of actively degrading ice wedge polygons that are present along a slightly elevated bench (∼ 3 m) in mixed forest. In this area, pockets of low-resistivity material in the upper 1–2 m denote the thawed areas around the high-centered polygons. Permafrost (1.2 m depth) temperatures at this location have increased steadily since 2013 and

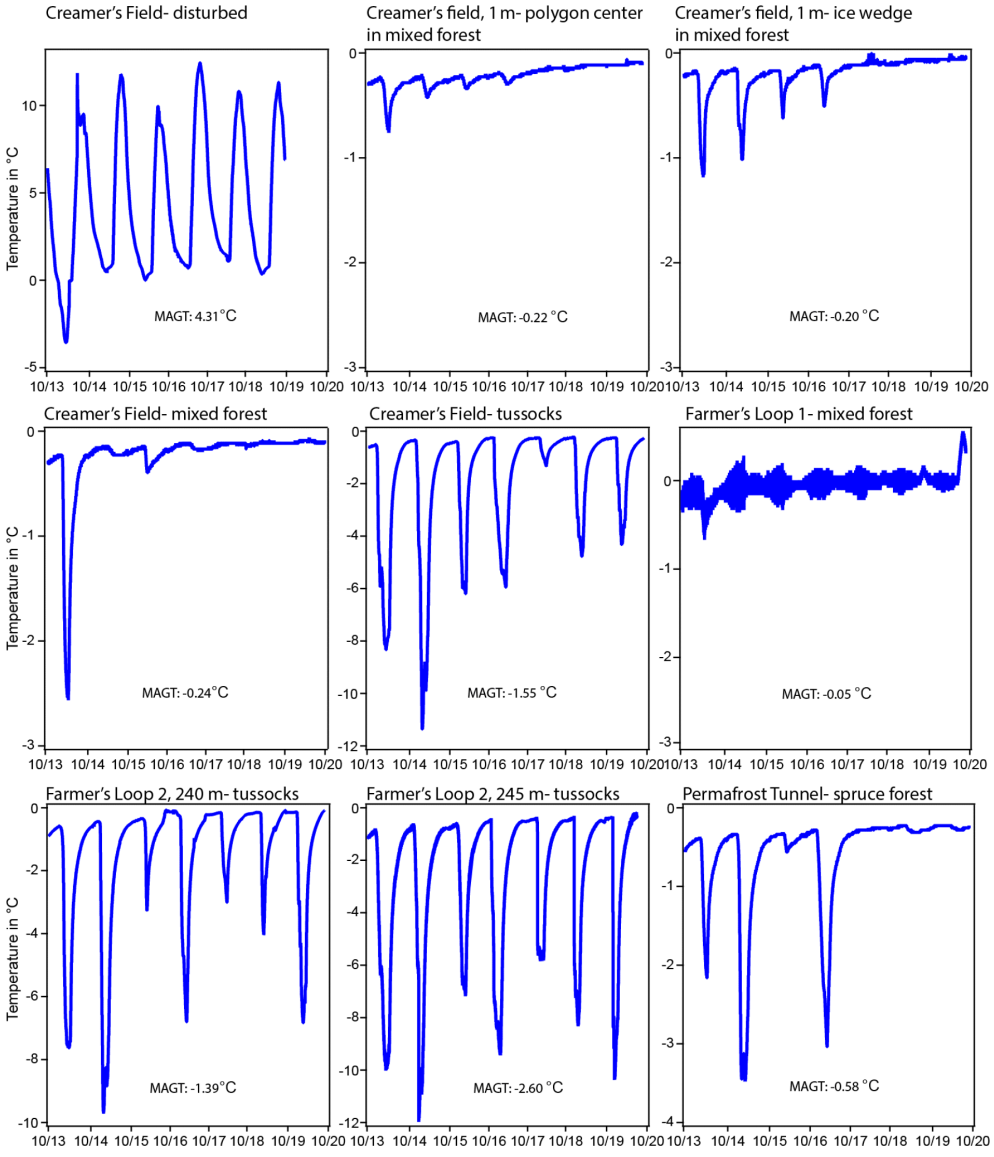

Figure 9. Soil temperature measurements at 1.2 m depth from 1 October 2013 to 1 October 2019 for the three study sites. Mean annual ground temperature (MAGT) values at 1.2 m for the period of record are also provided.

are currently only slightly below freezing (Fig. 9). This is the same region that exhibits the largest rates of ground subsidence in repeat lidar differencing at the site (Fig. 7). The greatest active layer depths along the Creamer's Field transect are located in this area. It is noteworthy that at some locations along this segment of the transect the seasonal thaw depth expanded $\sim 25\,\%$ between late August and early October. Clearly the permafrost along the first ~ 75 m of the transect is undergoing active thaw degradation. At 140 m along the transect the ground surface elevation is slightly lower and from there to the end of the transect the ecotype is characterized as tussock tundra. The permafrost in the tussock region is colder (MAGT at 1.2 m: $-1.55\,^{\circ}\mathrm{C}$) with little increase in thaw depth between late August and early October. The lone exception is a small (2–5 m across) thermokarst feature at a transect distance of 380 m that exhibits anomalous thaw throughout the summer and is discernible in the aerial image, lidar, and ERT measurements.

Both of the Farmer's Loop transects (Figs. 4 and 5) start in a mixed forest for the first ~ 125 m. In this area the near-surface permafrost is comprised of silts with minor peat and some layers with low gravimetric moisture contents of ~ 23–$50\ \mathrm{g\,g^{-1}}$. These areas also have the deepest active layer depths. Some small thawed areas as well as disturbed areas and small wetland features are identifiable by resistivity values of 200–700 Ω m in the upper few meters and active layers more than a meter deep. As with the Creamer's Field site, these ecotypes are associated with the largest increase in ac-

tive layer depth between late August and early October. Permafrost in this area appears to be present for only the upper 15 to 20 m. A small flow through fen from 120 to 180 m along Farmer's Loop 2 transect has a low-resistivity region ∼ 15 m below the ground surface. These areas are associated with the warmest permafrost temperatures at the Farmer's Loop site (−0.05 °C at 1.2 m; Fig. 9; Table 2).

Once the transect transitions into tussock tundra, the active layer depths become shallower and the temperatures at 1.2 m decrease. Regions of anomalously low ERT measurements are associated with small surface thermokarst features, water features, or disturbed areas. Soils in the area are characterized as silts with varied ice contents. A deep drill hole at 358 m along Farmer's Loop 1 transect identified thawed material starting at 9.15 m, and this corresponds with the marked decrease in resistivity values at this same location and depth.

At the Permafrost Tunnel site (Fig. 6) the ERT resistivity values are 1000 to 2000 Ω m in the upper ∼ 4 m with a repeating pattern of markedly higher values (5000 to 10 000 Ω m) from 4 to 10 m in depth and at a ∼ 10 m spacing. This is consistent with ice wedge polygon structures in the subsurface, likely the "upper silt unit" overlain by Holocene silts as mapped by Hamilton et al. (1988) and corroborated by our core drilling at the site. These subsurface ice wedge structures do not extend to the surface, and, as such, they do not relate to vegetation type or seasonal thaw depth changes across the transect. Towards the far end of the Permafrost Tunnel transect the ERT from 2014 identifies the lateral edges of a large thermokarst feature forming at the site. Thaw between 2014 and 2020 has added roughly 25 m of width to both sides of the feature.

5 Discussion

The results from this study clearly show, through a variety of corroborating measurements, ice-rich yedoma permafrost in the area around Fairbanks, Alaska, has been warming and actively degrading in numerous locations. Four major lines of evidence show permafrost thaw degradation has been initiated and is likely increasing at our sites. First, active layer measurements show thaw depths have been increasing across all ecotypes since 2013 (Table 1); however, some ecotypes experience deeper seasonal thaw than others. In 2014, the only year when we made repeat thaw depth measurements during the summer (Figs. 2–6c and d), it is apparent that in mid-June there is minimal variability in thaw depth except for some of the disturbed areas that eventually exhibit the deepest active layer thickness. By mid-July the disturbed and mixed-forest ecotypes exhibit the most seasonal thaw, and these ecotypes have the deepest end of season active layer depth measurements. In some locations, particularly the disturbed sites, mid-August seasonal thaw depths and early October active layer measurements show a ∼ 20 % increase over that 6-week period. The length of the summer growing season in the area has increased by 38 d (Wendler and Shulski, 2009), and our thermistor measurements (Fig. 9) show peak soil temperatures at 1.2 m typically occur in late November. From this, it is clear that the timing of thaw depth measurements may have to be pushed later into the fall to adequately represent the entire thaw season, particularly in mixed-forest and wetland ecotypes (Figs. 2–6). This has ramifications for field studies where thaw depth measurements are made in August during the end of most field seasons, as these measurements will increasingly underrepresent the maximum depth of thaw.

Previous studies have established that vegetation provides a range of "ecosystem protection" properties for permafrost (Shur and Jorgenson, 2007; Loranty et al., 2018). Recent measurements confirm this and identify strong links between different ecotypes and top-down thaw of permafrost in interior Alaska (Yi et al., 2018; Douglas et al., 2020; Jorgenson et al., 2020; Kropp et al., 2020). In this study, some ecotypes are associated with consistently deeper active layer measurements over time. Disturbances, like trail crossings, are associated with dramatically deeper seasonal thaw than any other ecotypes, and some of them are also expanding laterally. Removal or alteration of the organic soil layer or moss ground cover increases the ground heat flux and promotes more rapid seasonal and permafrost thaw (Nicholas and Hinkel, 1996) due to the loss of the ecosystem protection of permafrost in the area (Shur and Jorgenson, 2007). In many locations at our field sites, active layer depths have increased since 2013 to greater than 2 m, which is greater than typical winter freezeback. Infrastructure development and wildfire are the most likely ways for land cover to change to a disturbed ecotype. Post-fire forest succession to a mixed forest, which is increasingly occurring across interior Alaska and much of the boreal biome, will also undoubtedly lead to warmer surface soils and more top-down permafrost thaw (Kasischke and Johnstone, 2005; Johnstone et al., 2010; Jafarov et al., 2013; Brown et al., 2015). Tussock tundra and some of the spruce forest sites yield the shallowest active layer depths. As such, if vegetation were to change from tussocks or spruce to a mixed-forest or disturbed (i.e., no moss or forest vegetation) land cover, the potential risk of top-down permafrost thaw would increase considerably.

Our results support recent work at our study sites that show the disturbed, mixed-forest, and wetland ecotypes exhibit the deepest active layers (Douglas et al., 2020). That study presents measurements from 2014 to 2017 at the same sites presented here and links deeper active layer depths with wetter summers. The 4 additional years presented here show the thaw front has continued to migrate downward despite the lack of anomalously wet summers in 2018 and 2019. At most sites the 2020 active layer depths are the deepest in the record, and the comparatively shallower thaw depths measured in 2013 have not been repeated at any site since then.

The increase in active layer depths we measured at our sites since 2013 is similar to the longer-term trend rep-

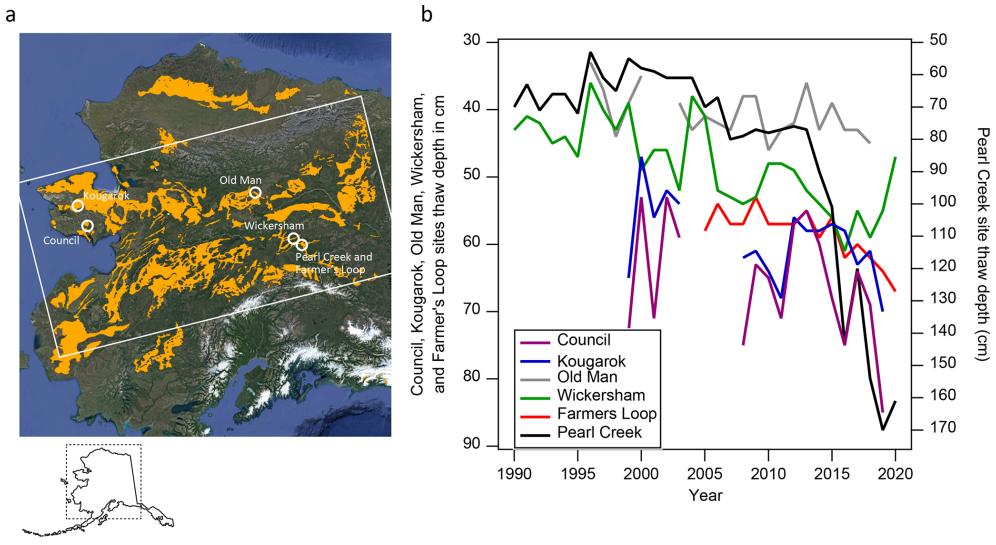

Figure 10. (a) A © Google Earth map identifying yedoma-type permafrost (yellow) in Alaska (Strauss et al., 2016) and locations of six central Alaska Circumpolar Active Layer Monitoring sites with records of at least 15 years. The focused field sites in this study are all near Farmer's Loop. The white bounding box represents the 500 000 km^2 area of central Alaska across which the study measurements are extrapolated. **(b)** Active layer measurements from the six CALM sites from interior Alaska and the Seward Peninsula. Data from CALM (2020).

resented at all six Circumpolar Active Layer Monitoring sites spread across 500 000 km^2 of central Alaska (the east–west swath south of the Brooks Range and north of the Alaska Range; Fig. 10; CALM, 2020). At most sites a steady increase in active layer depth was initiated around 2010 and has continued since. Within this region of central Alaska 159 000 km^2 of the permafrost has been identified as yedoma. This represents roughly 25 % of the total global yedoma permafrost area of 625 000 km^2 (Strauss et al., 2016). Using the regions mapped as yedoma to select the corresponding areas from ecotype maps that cover all of central Alaska (Jorgenson and Meidlinger, 2015; Raynolds et al., 2019), we calculate the five ecotypes in our study to represent 90 % of the total land cover on top of yedoma permafrost. Mixed forest (34 %), moss–spruce forest (23 %), wetland (20 %), and tussock tundra (13 %) are widely prevalent while disturbed sites are not identified, likely due to their small spatial scale. Using the total 2013–2020 increase in active layer depth from our field measurements in central Alaska ecotypes, projecting the area of each ecotype across the central Alaska domain mapped as yedoma, and using the mean organic carbon concentration in Siberian and Alaskan yedoma permafrost of 10 kg m^{-3} from Strauss et al. (2013), we calculate a first-order estimate of the total central Alaska yedoma permafrost organic carbon (OC) pool that has thawed since 2013 as 0.44 Pg OC. This estimate does not include non-yedoma permafrost in the same region that likely has also thawed since 2013.

Additional evidence indicating thaw of near-surface permafrost at our sites includes some thermistor measurements approaching and eventually warming above 0 °C at 1.2 m depth (Fig. 8) at some sites. Mixed-forest sites have warmed the most, and all three of our 1.2 m deep thermistors in this ecotype exhibit a steady warming that has been retarded at ~ -0.1 °C, likely due to latent heat effects associated with the phase change of ground ice in the transient layer and below (Boike et al., 1998; Shur et al., 2005). The tussock and spruce forest ecotypes do not show the steady increases in permafrost temperatures; however, the overall trend in mean annual temperatures at 1.2 m depth at these sites is increasing (Table 2).

The third indication of near-surface permafrost thaw and lowering of the permafrost table is the widespread development of a permanent residual thaw layer between the top of permafrost and the base of seasonally frozen ground at our sites indicated by SIPRE cores collected in 2017 and 2018. At many locations, the seasonal thaw has proven to be deeper than the depth of winter freezeback. Residual thaw layers are located predominantly in the mixed-forest and disturbed ecotypes. These areas contain the warmest near-surface permafrost, and in some cases the low ice content sandy silts have a higher thermal conductivity that promotes the movement of heat into the ground. At some of these sites where the thaw front has penetrated to a depth of 1.2 m, we have had to augment the instrumentation by installing deeper thermistors (i.e., 2 to 2.5 m) to maintain temperature measurements of the near-surface permafrost. Since thaw depths increased in 2019 and 2020, it is likely residual thaw layers have increased in thickness and lateral extent. At locations where the thaw front has extended below 1.5 to 2 m it is likely that taliks have formed.

Numerous lines of visual evidence provide the fourth indication of active permafrost thaw in our research area. The most dramatic is that of the ground subsidence associated with permafrost thaw in the mixed-forest region of the Creamer's Field transect (Fig. 9). Ice wedge polygons in the area have warmed steadily since 2013, and repeat lidar analysis shows high-centered polygon development has expanded due to melting ice wedges (Fig. 7). This suggests potential hydrologic and soil thermal process changes are ongoing in that area (Liljedahl et al., 2016). Anomalous thaw depths coinciding with recent development of thermokarst pits are evident in airborne lidar and true-color images at all of our sites. At the Creamer's Field site, degradation of ice wedge polygons is evident in our repeat lidar analysis, and the most striking thaw subsidence occurred in the mixed-forest area along the first 150 m of this transect. The near-surface permafrost soils in this area, comprised of lower ice content silts and sands, are warmer than nearby permafrost overlain by tussocks, and high-centered polygons had already begun to develop before we initiated our study. Some of the low-lying troughs between polygons, particularly those along the thaw front next to the ponded area to the west, have settled by 1–1.5 m in the decade from 2010 to 2020. For some areas in the vicinity of this transect, ground elevations of the polygon troughs increased between 2010 and 2020, but we attribute this to the area being extremely low-lying and to more standing water in the troughs from greater snowmelt in May 2020 compared to that in 2010. Due to this standing water we could not ascertain whether the ice wedges in this area had melted or not.

Our study further confirms recent studies showing ERT measurements provide a robust way to characterize frozen versus thawed zones in permafrost terrains (Lewkowicz et al., 2011; Hubbard et al., 2013; Minsley et al., 2016; Douglas et al., 2008, 2016; Rey et al., 2020; Bjella, 2014, 2015, 2020). High-resistivity areas identify permafrost while low resistivity values correspond with thawed zones at the surface. Hotspots of low resistivity values correspond with deep active layer measurements, for example, at disturbed sites and across thermokarst features where thaw is identifiable from airborne imagery and lidar. Few studies have coupled ERT measurements with deep boreholes to corroborate the bottom or lateral extent of permafrost, yet mapping these 0 °C isotherm boundaries is critical for tracking and modeling lateral and top-down thaw. At the 358 m distance on the Farmer's Loop 1 transect, our borehole encountered a thawed zone at $\sim$ 10 m that corresponds exactly with the bottom of frozen soil measured by the large decrease in resistivity at that location (Fig. 4). Our ERT results show discontinuous permafrost is present at depths of up to at least 25 m across all transects, but the lateral extent of small surface and subsurface thawed regions (as of 2014) is identifiable in ERT measurements at all sites.

The deep boreholes, in some cases representing the bottom of permafrost where bottom-up thaw is occurring (McClymont et al., 2013), also provided access to wooden fragment samples amenable for ^{14}C dating. Based on the relationship between core depth and age date at the three locations where we have ^{14}C ages, we calculate vertical accumulation of syngenetic permafrost at rates of 0.7 to 1 mm yr^{-1}. This is close to the rates measured in the Permafrost Tunnel (Hamilton et al., 1988), and these rates are important for mapping and modeling permafrost lateral and vertical extent across remote locations.

6 Conclusions

The variety of measurements used in this study all confirm that near-surface permafrost around Fairbanks, Alaska, has been undergoing marked warming and widespread thermokarst development since our measurements started in 2013. The majority of the warming and thaw degradation are occurring in mixed-forest ecotypes with low-ice-content sandy-silt soils; however, remote sensing evidence shows thermokarst features, including bog initiation, pits, troughs, sinkholes, irregular depressions and mounds, and moats, have been initiated in all of the ecotypes represented. Even though the tussock tundra and spruce forest ecotypes have the lowest mean annual near-surface permafrost temperatures at 1.2 m depth, they exhibit long-term increases in ground temperatures. Whereas these sites achieve the lowest minimum 1.2 m ground temperatures among all of our sites, winter processes may control the potential future thermal state of permafrost below these ecotypes. Based on CALM site measurements, mapping, and geospatial analyses, we conclude the rapid and extensive thaw we identified at our field sites is likely common across the 500 000 km^2 area of central Alaska. Since the yedoma-type permafrost at our field sites and across the larger region is ice-rich and has a high carbon content, there is high risk of thaw degradation and impacts to the carbon cycle. Based on our first-order calculations, the total central Alaska yedoma permafrost organic carbon (OC) pool that has thawed since 2013, and which is now available to the carbon cycle, is approximately 0.44 Pg OC. For perspective, this is slightly more mass than the yearly CO_2 emissions of Australia (Friedlingstein et al., 2019). Results from this study can support large-scale modeling efforts on how current and projected future land cover will armor permafrost against thaw and disturbance and also how and where ecotype changes can increase the risk of permafrost thaw and thermokarst development. Our study sites are well suited to support these types of analyses because the area contains warm permafrost, the climate has been warming since the 1970s, and our transects represent most of the land cover present in the boreal and taiga of the Arctic and subarctic. The relationships we found between ecotype, permafrost composition, and seasonal thaw dynamics can be used to apply biophysical characteristics and standoff measurements like repeat aerial imagery, hyperspectral measurements, and

lidar to ascertain the presence or absence of permafrost in similar terrains. This will help improve three-dimensional thermal modeling of top-down, lateral, and bottom-up thaw of discontinuous permafrost bodies so future climate projections can better be applied toward identifying the likely response of permafrost to warming.

Data availability. Repeat seasonal thaw depth measurements (2014), repeat active layer measurements (2014–2020), and yedoma area carbon content calculations are available through Zenodo using https://doi.org/10.5281/zenodo.4670463 (Douglas, 2021). All project geophysical data are available through reasonable request.

Supplement. The supplement related to this article is available online at: https://doi.org/10.5194/tc-15-3555-2021-supplement.

Author contributions. TAD, CAH, and JEA designed and initiated the study and performed fieldwork. RAB, KLB, EJD, ABG, SDN, SPS, and AMW assisted in the field and analyzed data. PEN oversaw geospatial and mapping analyses. All authors contributed to development and writing of this paper.

Competing interests. The authors declare that they have no conflict of interest.

Disclaimer. Publisher's note: Copernicus Publications remains neutral with regard to jurisdictional claims in published maps and institutional affiliations.

Acknowledgements. We thank Amanda Barker, Sam Beal, Marc Beede, Maria Berkeland, Dana Brown, Seth Campbell, Jarrod Edwards, Tiffany Gatesman, Malcom Major, Margaret Rudolph, Torre Jorgenson, Merritt Turetsky, Simone Whitecloud, and Caiyun Zhang for help with field measurements. We appreciate comments about yedoma studies from Jens Strauss and acknowledge the two diligent reviewers and the editor Peter Morse for their constructive comments on multiple versions of the paper.

Financial support. This research was funded by the U.S. Army Corps of Engineers Engineer Research and Development Center Basic Research Program under PE 0601102/AB2 (Protection, Maneuver, Geospatial, Natural Sciences) and Center Directed Research Program and the Department of Defense's Strategic Environmental Research and Development Program (projects RC-2110 and RC18-1170).

Review statement. This paper was edited by Peter Morse and reviewed by Sebastian Wetterich and one anonymous referee.

References

Bjella, K.: Dalton Highway 9 to 11 Mile Expedient Resistivity Permafrost Investigation, Alaska Department of Transportation and Public Facilities Technical Report, FHWA-AK-RD-13-08, Fairbanks, Alaska, 2014.

Bjella, K.: Imaging of Ground Ice with Surface Based Geophysics, ERDC/CRREL Technical Report TR-15-14, Hanover, USA, 2015.

Bjella, K.: Improving Design Methodologies and Assessment Tools for Building on Permafrost in a Warming Climate, ERDC/CRREL Technical Report TR-20-13, Hanover, USA, 2020.

Boike, J., Roth, K., and Overduin, P. P.: Thermal and hydrologic dynamics of the active layer at a continuous permafrost site (Taymyr Peninsula, Siberia), Water Resour. Res., 34, 355–363, 1998.

Bray, M. T., French, H. M., and Shur, Y.: Further cryostratigraphic observations in the CRREL permafrost tunnel, Fox, Alaska, Permafrost Periglac. Process., 17, 233–243, 2006.

Brown, D. R. N., Jorgenson, M. T., Douglas, T. A., Romanovsky, V., Kielland, K., and Euskirchen, E.: Vulnerability of permafrost to fire-initiated thaw in lowland forests of the Tanana Flats, interior Alaska, J. Geophys. Res.-Biogeo., 120, 1619–1637, https://doi.org/10.1002/2015JG003033, 2015.

Burkert A., Douglas T. A., Waldrop, M. P., and Mackelprang, R.: Changes in the active, dead, and dormant microbial community structure across a Pleistocene permafrost chronosequence, Appl. Environ. Microbio., 85, e02646-18, https://doi.org/10.1128/AEM.02646-18, 2019.

Chasmer, L. and Hopkinson, C.: Threshold loss of discontinuous permafrost and landscape evolution, Glob. Change Biol., 23, 2672–2686, https://doi.org/10.1111/gcb.13537, 2017.

Circumpolar Active Layer Monitoring Network: https://www2.gwu.edu/~calm/data/north.htm (last access: 11 June 2021), 2020.

Douglas, T. A.: Repeat active layer depths at sites near Fairbanks, Alaska (Version 1), Zenodo [data set], https://doi.org/10.5281/zenodo.4670463, 2021.

Douglas, T. A. and Mellon, M. T.: Sublimation of terrestrial permafrost and the implications for ice-loss processes on Mars, Nature Comm., 10, 1716, https://doi.org/10.1038/s41467-019-09410-8, 2019.

Douglas, T. A., Jorgenson, M. T., Kanevskiy, M. Z., Romanovsky, V. E., Shur, Y., and Yoshikawa, K.: Permafrost dynamics at the Fairbanks Permafrost Experimental Station near Fairbanks, Alaska, Proceedings of the Ninth International Conference on Permafrost, edited by: Kane, D. and Hinkel, K., University of Alaska Fairbanks, 29 June–3 July 2008.

Douglas, T. A., Fortier, D., Shur, Y. I., Kanevskiy, M. Z., Guo, L., Cai, Y., and Bray, M.: Biogeochemical and geocryological characteristics of wedge and thermokarst-cave ice in the CRREL Permafrost Tunnel, Alaska, Permafrost Periglac. Process., 22, 120–128, https://doi.org/10.1002/ppp.709, 2011.

Douglas, T. A., Blum, J. D., Guo, L., Keller, K., and Gleason, J. D.: Hydrogeochemistry of seasonal flow regimes in the Chena River, a subarctic watershed draining discontinuous permafrost in interior Alaska (USA), Chem. Geol., 335, 48–62, 2013.

Douglas, T. A., Jones, M. C., Hiemstra, C. A., and Arnold, J.: Sources and sinks of carbon in boreal ecosystems of Interior Alaska: Current and future per-

spectives for land managers, Elementa, 2, 000032, https://doi.org/10.12952/journal.elementa.000032, 2014.

Douglas, T. A., Jorgenson, M. T., Brown, D. R. N., Campbell, S. W., Hiemstra, C. A., Saari, S. P., Bjella, K., and Liljedahl, A. K.: Degrading permafrost mapped with electrical resistivity tomography, airborne imagery and LiDAR, and seasonal thaw measurements, Geophysics, 81, WA71–WA85, https://doi.org/10.1190/GEO2015-0149.1, 2016.

Douglas, T. A., Turetsky, M. R., and Koven, C. D.: Increased rainfall stimulates permafrost thaw across a variety of Alaskan ecosystems, npj Climate Atmos. Sci., 3, 1–7, 2020.

Friedlingstein, P., Jones, M. W., O'Sullivan, M., Andrew, R. M., Hauck, J., Peters, G. P., Peters, W., Pongratz, J., Sitch, S., Le Quéré, C., Bakker, D. C. E., Canadell, J. G., Ciais, P., Jackson, R. B., Anthoni, P., Barbero, L., Bastos, A., Bastrikov, V., Becker, M., Bopp, L., Buitenhuis, E., Chandra, N., Chevallier, F., Chini, L. P., Currie, K. I., Feely, R. A., Gehlen, M., Gilfillan, D., Gkritzalis, T., Goll, D. S., Gruber, N., Gutekunst, S., Harris, I., Haverd, V., Houghton, R. A., Hurtt, G., Ilyina, T., Jain, A. K., Joetzjer, E., Kaplan, J. O., Kato, E., Klein Goldewijk, K., Korsbakken, J. I., Landschützer, P., Lauvset, S. K., Lefèvre, N., Lenton, A., Lienert, S., Lombardozzi, D., Marland, G., McGuire, P. C., Melton, J. R., Metzl, N., Munro, D. R., Nabel, J. E. M. S., Nakaoka, S.-I., Neill, C., Omar, A. M., Ono, T., Peregon, A., Pierrot, D., Poulter, B., Rehder, G., Resplandy, L., Robertson, E., Rödenbeck, C., Séférian, R., Schwinger, J., Smith, N., Tans, P. P., Tian, H., Tilbrook, B., Tubiello, F. N., van der Werf, G. R., Wiltshire, A. J., and Zaehle, S.: Global Carbon Budget 2019, Earth Syst. Sci. Data, 11, 1783–1838, https://doi.org/10.5194/essd-11-1783-2019, 2019.

Grosse, G., Harden, J., Turetsky, M., McGuire, A. D., Camill, P., Tarnocai, C., Frolking, S., Schuur, E. A., Jorgenson, T., Marchenko, S., and Romanovsky, V.: Vulnerability of high-latitude soil organic carbon in North America to disturbance, J. Geophys. Res.-Biogeosci., 116, G00K06, https://doi.org/10.1029/2010JG001507, 2011.

Hamilton, T. D., Craig, J. L., and Sellmann, P. V.: The Fox permafrost tunnel: A late Quaternary geologic record in central Alaska, Geol. Soc. Amer. Bull., 100, 948–969, 1988.

Harada, K. and Yoshikawa, K.: Permafrost age and thickness near Adventfjorden, Spitsbergen, Polar Geography, 20, 267–281, 1996.

Harada, K., Wada, K., and Fukuda, M.: Permafrost mapping by transient electromagnetic method, Permafrost Periglac. Process., 11, 71–84, 2000.

Heslop, J. K., Winkel, M., Walter Anthony, K. M., Spencer, R. G., Podgorski, D. C., Zito, P., Kholodov, A., Zhang, M., and Liebner, S.: Increasing organic carbon biolability with depth in yedoma permafrost: ramifications for future climate change, J. Geophys. Res.-Biogeosci., 124, 2021–2038, 2019.

Hinkel, K. M. and Nelson, F. E.: Spatial and temporal patterns of active layer thickness at Circumpolar Active Layer Monitoring (CALM) sites in northern Alaska, 1995–2000, J. Geophys. Res., 108, 8168, https://doi.org/10.1029/2001JD000927, 2003.

Hjort, J., Karjalainen, O., Aalto, J. Westermann, S., Romanovsky, V. E., Nelson, F. E., Etzelmüller, B., and Luoto, M.: Degrading permafrost puts Arctic infrastructure at risk by mid-century, Nat. Comm., 9, 5147, https://doi.org/10.1038/s41467-018-07557-4, 2018.

Hoekstra, P.: Electromagnetic probing of permafrost, in: Proceedings of 2nd International Conference on Permafrost, Yakutsk, USSR, North American Contribution, National Academy of Science, 517–526, 1973.

Hubbard, T. D., Braun, M. L., Westbrook, R. E., and Gallagher, P. E.: High-resolution lidar data for infrastructure corridors, Fairbanks Quadrangle, Alaska, in: High-resolution lidar data for Alaska infrastructure corridors, edited by: Hubbard, T. D., Koehler, R. D., and Combellick, R. A., Alaska Division of Geological & Geophysical Surveys Raw Data File 2011-3E, https://doi.org/10.14509/22727, 2011.

Hubbard, S. S., Gangodagamage, C., Dafflon, B., Wainwright, H., Peterson, J., Gusmeroli, A., Ulrich, C., Wu, Y., Wilson, C., Rowland, J., Tweedie, C., and Wullscheleger, S. D.: Quantifying and relating land-surface and subsurface variability in permafrost environments using LiDAR and surface geophysical datasets, Hydrogeol. J., 21, 149–169, 2013.

Jafarov, E. E., Romanovsky, V. E, Genet, H., McGuire, A. D., and Marchenko, S. S.: The effects of fire on the thermal stability of permafrost in lowland and upland black spruce forests of interior Alaska in a changing climate, Environ. Res. Lett., 8, 035030, https://doi.org/10.1088/1748-9326/8/3/035030, 2013.

Johnstone, J. F., Chapin, F. S., Hollingsworth, T. N., Mack, M. C., Romanovsky, V., and Turetsky, M.: Fire, climate change, and forest resilience in interior Alaska, Can. J. Forest Res., 40, 1302–1312, 2010.

Jones, B. M., Stoker, J. M., Gibbs, A. E., Grosse, G., Romanovsky, V. E., Douglas, T. A., Kinsman, N. E. M., and Richmond, B. M.: Quantifying landscape change in an arctic coastal lowland using repeat airborne LiDAR, Environ. Res. Lett., 8, 045025, https://doi.org/10.1088/1748-9326/8/4/045025, 2013.

Jorgenson, M. T., Racine, C. H., Walters, J. C., and Osterkamp, T. E.: Permafrost degradation and ecological changes associated with a warming climate in central Alaska, Clim. Change, 48, 551–579, 2001.

Jorgenson, M. and Osterkamp, T.: Response of boreal ecosystems to varying modes of permafrost degradation, Can. J. For. Res., 35, 2100–2111, 2005.

Jorgenson, M. T., Yoshikawa, K., Kanevskiy, M., Shur, Y., Romanovsky V., Marchenko, S., Grosse, G., Brown, J., and Jones, B.: Permafrost characteristics of Alaska, Proceedings of the Ninth International Conference on Permafrost, edited by: D. Kane, and K. Hinkel, University of Alaska Fairbanks, 29 June–3 July 2008, vol. 29, 121–122, 2008.

Jorgenson, M. T., Harden, J., Kanevskiy, M., O'Donnell, J., Wickland, K., Ewing, S., Manies, K., Zhuang, Q., Shur, Y., Striegl, R., and Koch, J.: Reorganization of vegetation, hydrology and soil carbon after permafrost degradation across heterogeneous boreal landscapes, Environ. Res. Lett., 16, 8, 035017, https://doi.org/10.1088/1748-9326/8/3/035017, 2013.

Jorgensen, T. and Meidlinger, D.: The Alaska Yukon Region of the Circumboreal Vegetation map (CBVM), Conservation of Arctic Flora and Fauna (CAFF), available at: https://www.caff.is/strategies-series/359-the-alaska-yukon-region-of-the-circumboreal-vegetation-map-cbvm (last access: 11 February 2021), 2015.

Jorgenson, M. T., Douglas, T. A., Liljedahl, A. K., Roth, J. E., Cater, T. C., Davis, W. A., Frost, G. V., Miller, P. F., and Racine, C. H.: The roles of climate extremes, ecological succession, and hydrol-

ogy in cycles of permafrost aggradation and degradation in fens on the Tanana Flats, Alaska, J. Geophys. Res.-Biogeosci., 125, e2020JG005824, https://doi.org/10.1029/2020JG005824, 2020.

Kanevskiy, M., Shur, Y., Fortier, D., Jorgenson, M. T., and Stephani, E.: Cryostratigraphy of late Pleistocene syngenetic permafrost (yedoma) in northern Alaska, Itkillik River exposure, Quat. Res., 75, 584–596, 2011.

Kasischke, E. S. and Johnstone, J. F.: Variation in postfire organic layer thickness in a black spruce forest complex in interior Alaska and its effects on soil temperature and moisture, Can. J. For. Res., 35, 2164–2177, 2005.

Kneisel, C.: Assessment of subsurface lithology in mountain environments using 2D resistivity imaging, Geomorphol., 80, 32–44, 2006.

Kokelj, S. V. and Jorgenson, M. T.: Advances in Thermokarst Research, Permafrost Periglac. Process., 24, 108–119, 2013.

Kropp, H., Loranty, M. M., Natali, S. M., Kholodov, A. L., Rocha, A. V., Myers-Smith, I., Abbot, B. W., Abermann, J., Blanc-Betes, E., Blok, D., Blume-Werry, G., Boike, J., Breen, A. L., Cahoon, S. M. P., Christiansen, C. T., Douglas, T. A. Epstein, H. E., Frost, G. V., Goeckede, M., Høye, T. T., Mamet, S. D., O'Donnell, J. A., Olefeldt, D., Phoenix, G. K., Salmon, V. G., Sannel, A. B. K., Smith, S. L., Sonnentag, O., Vaughn, L. S., Williams, M., Elberling, B., Gough, L., Hjort, J., Lafleur, P. M., Euskirchen, E. S., Heijmans, M. M. P. D., Humphreys, E. R., Iwata, H., Jones, B. M., Jorgenson, M. T., Grünberg, I., Kim, Y., Laundre, J., Mauritz, M., Michelsen, A., Schaepman-Strub, G., Tape, K. D. Ueyama, M., Lee, B.-Y., Langley, K., and Lund, M.: Vegetation stature controls air-soil temperature coupling across pan-Arctic ecosystems, Environ. Res. Lett., 85, 015001, https://doi.org/10.1088/1748-9326/abc994, 2020.

Lader, R., Walsh, J. E., Bhatt, U. S., and Bieniek, P. A.: Projections of twenty-first-century climate extremes for Alaska via dynamical downscaling and quantile mapping, J. Appl. Meteorol. Climatol., 56, 2393–2409, 2017.

Latifovic, R., Pouliot, D., and Olthof, I.: Circa 2010 Land Cover of Canada: Local Optimization Methodology and Product Development, Rem. Sens., 9, 1098, https://doi.org/10.3390/rs9111098, 2017.

Lewkowicz, A. G. and Way, R. G.: Extremes of summer climate trigger thousands of thermokarst landslides in a High Arctic environment, Nature Comm., 10, 1329, https://doi.org/10.1038/s41467-019-09314-7, 2019.

Lewkowicz, A. G., Etzelmüller, B., and Smith, S. L.: Characteristics of discontinuous permafrost based on ground temperature measurements and electrical resistivity tomography, southern Yukon, Canada, Permafrost Periglac. Process., 22, 320–342, 2011.

Liljedahl, A. K., Boike, J., Daanen, R. P., Fedorov, A. N., Frost, G. V., Grosse, G., Hinzman, L. D., Iijma, Y., Jorgenson, J. C., Matveyeva, N., and Necsoiu, M.: Pan-Arctic ice-wedge degradation in warming permafrost and its influence on tundra hydrology, Nature Geosci., 4, 312–318, 2016.

Liston, G. E. and Hiemstra, C. A.: The changing cryosphere: Pan-Arctic snow trends (1979–2009), J. Climate, 24, 5691–5712, 2011.

Loke, M. H. and Barker, R. D.: Rapid least-squares inversion of apparent resistivity pseudosections by a quasi-Newton method 1, Geophys. Prospect., 44, 131–152, 1996.

Loke, M. H., Acworth, I., and Dahlin, T.: A comparison of smooth and blocky inversion methods in 2D electrical imaging surveys, Exploration Geophys., 34, 182–187, 2003.

Loranty, M. M., Abbott, B. W., Blok, D., Douglas, T. A., Epstein, H. E., Forbes, B. C., Jones, B. M., Kholodov, A. L., Kropp, H., Malhotra, A., Mamet, S. D., Myers-Smith, I. H., Natali, S. M., O'Donnell, J. A., Phoenix, G. K., Rocha, A. V., Sonnentag, O., Tape, K. D., and Walker, D. A.: Reviews and syntheses: Changing ecosystem influences on soil thermal regimes in northern high-latitude permafrost regions, Biogeosciences, 15, 5287–5313, https://doi.org/10.5194/bg-15-5287-2018, 2018.

Mackelprang, R., Waldrop, M. P., DeAngelis, K. M., David, M. M., Chavarria, K. L., Blazewicz, S. J., Rubin, E. M., and Jansoon, J. K.: Metagenomic analysis of a permafrost microbial community reveals a rapid response to thaw, Nature, 480, 368–371, 2011.

Mackelprang, R., Burkert, A., Haw, M., Mahendrarajah, T., Conaway, C. H., Douglas, T. A., and Waldrop, M. P.: Microbial survival strategies in ancient permafrost: insights from metagenomics, ISME Journal, 11, 2305–2318, 2017.

McClymont, A. F., Hayashi, M., Bentley, L. R., and Christensen, B. S.: Geophysical imaging and thermal modeling of subsurface morphology and thaw evolution of discontinuous permafrost, J. Geophys. Res.-Earth Surf., 118, 1826–1837, 2013.

Messan, K. S., Jones, R. M., Doherty, S. J., Foley, K., Douglas, T. A., and Barbato, R. A.: The role of changing temperature in microbial metabolic processes during permafrost thaw, PloS one, 15, e0232169, https://doi.org/10.1371/journal.pone.0232169, 2020.

Minsley, B. J., Wellman, T. P., Walvoord, M. A., and Revil, A.: Sensitivity of airborne geophysical data to sublacustrine and near-surface permafrost thaw, The Cryosphere, 9, 781–794, https://doi.org/10.5194/tc-9-781-2015, 2015.

Minsley, B. J., Pastick, N. J., Wylie, B. K., Brown, D. R., and Kass, M. A.: Evidence for nonuniform permafrost degradation after fire in boreal landscapes, J. Geophys. Res.-Earth Surf., 121, 320–335, 2016.

Myers-Smith, I. H., Harden, J. W., Wilmking, M., Fuller, C. C., McGuire, A. D., and Chapin III, F. S.: Wetland succession in a permafrost collapse: interactions between fire and thermokarst, Biogeosciences, 5, 1273–1286, https://doi.org/10.5194/bg-5-1273-2008, 2008.

Neumann, R. B., Moorberg, C. J., Lundquist, J. D., Turner, J. C., Waldrop, M. P., McFarland, J. W., Euskirchen, E. S., Edgar, C. W., and Turetsky, M. R.: Warming effects of spring rainfall increase methane emissions from thawing permafrost, Geophysi. Res. Lett., 46, 1393–1401, 2019.

Nicholas, J. R. and Hinkel, K. M.: Concurrent permafrost aggradation and degradation induced by forest clearing, central Alaska, USA, Arctic, Ant., Alp. Res., 28, 294–299, 1996.

Nossov, D. R., Jorgenson, M. T., Kielland, K., and Kanevskiy, M. Z.: Edaphic and microclimatic controls over permafrost response to fire in interior Alaska, Environ. Res. Lett., 8, 035013, https://doi.org/10.1088/1748-9326/8/3/035013, 2013.

Osterkamp, T. and Romanovsky, V.: Evidence for warming and thawing of discontinuous permafrost in Alaska, Permafrost Periglac. Process., 10, 17–37, 1999.

Pastick, N. J., Jorgenson, M. T., Wylie, B. K., Nield, S. J., Johnson, K. D., and Finley, A. O.: Distribution of near-surface permafrost

in Alaska: Estimates of present and future conditions, Remote Sens. Environ., 168, 301–315, 2015.

Phillips, M. R., Burn, C. R., Wolfe, S. A., Morse, P. D., Gaanderse, A. J., O'Neill, H. B., Shugar, D. H., and Gruber, S.: Improving water content description of ice-rich permafrost soils, Proceedings of the 7th Canadian Permafrost Conference Québec City, 68, https://doi.org/10.13140/RG.2.1.4760.1126, 2015.

Racine, C. H. and Walters, J. C.: Groundwater-discharge fens in the Tanana Lowlands, Interior Alaska, USA, Arctic Alpine Res., 26, 418–426, 1994.

Raynolds, M. K., Walker, D. A., Balser, A., Bay, C., Campbell, M., Cherosov, M. M., Daniëls, F. J., Eidesen, P. B., Ermokhina, K. A., Frost, G. V., and Jedrzejek, B.: A raster version of the Circumpolar Arctic Vegetation Map (CAVM), Remote Sens. Environ., 232, 111297, https://doi.org/10.1016/j.rse.2019.111297, 2019.

Rey, D. M., Walvoord, M. A., Minsley, B. J., Ebel, B. A., Voss, C. I., and Singha, K.: Wildfire initiated talik development exceeds current thaw projections: Observations and models from Alaska's continuous permafrost zone, Geophys. Res. Lett., 47, e2020GL087565. https://doi.org/10.1029/2020GL087565, 2020.

Schuster, P. F., Schaefer, K. M., Aiken, G. R., Antweiler, R. C., Dewild, J. F., Gryziec, J. D., Gusmeroli, A., Hugelius, G., Jafarov, E., Krabbenhoft, D. P., and Liu, L.: Permafrost stores a globally significant amount of mercury, Geophys. Res. Lett., 45, 1463–1471, 2018.

Shiklomanov, N. I., Streletskiy, D. A., Nelson, F. E., Hollister, R. D., Romanovsky, V. E., Tweedie, C. E., Bockheim, J. G., and Brown, J.: Decadal variations of active-layer thickness in moisture-controlled landscapes, Barrow Alaska, J. Geophys. Res., 115, G00I04, https://doi.org/10.1029/2009JG001248, 2010.

Shur, Y. L., Hinkel, K. M., and Nelson, F. E.: The transient layer: Implications for geocryology and global-change science, Permafrost Periglac. Process., 16, 5–17, 2005.

Shur, Y. and Jorgenson, M.: Patterns of permafrost formation and degradation in relation to climate and ecosystems, Permafrost Periglac. Process., 18, 7–19, 2007.

Smith, L. C., Sheng, Y., MacDonald, G. M., and Hinzman, L. D.: Disappearing Arctic lakes, Science, 308, 1429–1429, 2005.

Strauss, J., Schirrmeister, L., Grosse, G., Wetterich, S., Ulrich, M., Herzschuh, U., and Hubberten, H. W.: The deep permafrost carbon pool of the Yedoma region in Siberia and Alaska, Geophys. Res. Lett., 40, 6165–6170, 2013.

Strauss, J., Laboor, S., and Fedorov, A. N.: Database of ice-rich Yedoma permafrost (IRYP), PANGAEA, https://doi.org/10.1594/PANGAEA.861733, 2016.

Strauss, J., Schirrmeister, L., Grosse, G., Fortier, D., Hugelius, G., Knoblauch, C., Romanovsky, V., Schädel, C., von Deimling, T. S., Schuur, E. A., and Shmelev, D.: Deep Yedoma permafrost: A synthesis of depositional characteristics and carbon vulnerability, Earth Sci. Rev., 172, 75–86, 2017.

Vonk, J. E., Mann, P. J., Dowdy, K. L., Davydova, A., Davydov, S. P., Zimov, N., Spencer, R. G., Bulygina, E. B., Eglinton, T. I., and Holmes, R. M.: Dissolved organic carbon loss from Yedoma permafrost amplified by ice wedge thaw, Environ. Res. Lett., 8, 035023, https://doi.org/10.1088/1748-9326/8/3/035023, 2013.

Walker, M. D., Wahren, C. H., Hollister, R. D., Henry, G. H., Ahlquist, L. E., Alatalo, J. M., Bret-Harte, M. S., Calef, M. P., Callaghan, T. V., Carroll, A. B., and Epstein, H. E.: Plant community responses to experimental warming across the tundra biome, P. Natl. Acad. Sci. USA, 103, 1342–1346, 2006.

Way, R. G., Lewkowicz, A. G., and Zhang, Y.: Characteristics and fate of isolated permafrost patches in coastal Labrador, Canada, The Cryosphere, 12, 2667–2688, https://doi.org/10.5194/tc-12-2667-2018, 2018.

Wendler, G. and Shulski, M.: A century of climate change for Fairbanks, Alaska, Arctic, 62, 295–300, 2009.

Wilhelm, R. C., Niederberger, T. D., Greer, C., and Whyte, L. G.: Microbial diversity of active layer and permafrost in an acidic wetland from the Canadian High Arctic, Can. J., Microbiol., 57, 303–315, 2011.

Wolken, J. M., Hollingsworth, T. N., Rupp, T. S., Chapin III, F. S., Trainor, S. F., Barrett, T. M., Sullivan, P. F., McGuire, A. D., Euskirchen, E. S., Hennon, P. E., and Beever, E. A.: Evidence and implications of recent and projected climate change in Alaska's forest ecosystems, Ecosphere, 2, 1–35, 2011.

Yi, Y., Kimball, J. S., Chen, R. H., Moghaddam, M., Reichle, R. H., Mishra, U., Zona, D., and Oechel, W. C.: Characterizing permafrost active layer dynamics and sensitivity to landscape spatial heterogeneity in Alaska, The Cryosphere, 12, 145–161, https://doi.org/10.5194/tc-12-145-2018, 2018.

Yoshikawa, K. and Hinzman, L. D.: Shrinking thermokarst ponds and groundwater dynamics in discontinuous permafrost near Council, Alaska, Permafrost Periglac. Proc., 14, 151–160, 2003.

Yoshikawa, K., Leuschen, C., Ikeda, A., Harada, K., Gogineni, P., Hoekstra, P., Hinzman, L., Sawada, Y., and Matsuoka, N.: Comparison of geophysical investigations for detection of massive ground ice (pingo ice), J. Geophys. Res.-Planets, 111, E06S19, https://doi.org/10.1029/2005JE002573, 2006.